Physics of Fluids

RESEARCH ARTICLE | MAY 25 2023

Heat transfer effects on multiphase Richtmyer–Meshkov instability of dense gas–particle flow

Si Yingming (司英明) ; Li Shuai (李帅) ; Chen Qian (陈潜); Meng Baoqing (孟宝清) ;
Wang Chun (王春) ; Tian Baolin (田保林)

Physics of Fluids 35, 053339 (2023)
https://doi.org/10.1063/5.0149563

Physics of Fluids ARTICLE pubs.aip.org/aip/pof

Heat transfer effects on multiphase Richtmyer–Meshkov instability of dense gas–particle flow

Cite as: Phys. Fluids **35**, 053339 (2023); doi: 10.1063/5.0149563
Submitted: 7 March 2023 · Accepted: 8 May 2023 ·
Published Online: 25 May 2023

Yingming Si (司英明),[1,2] Shuai Li (李帅),[3,4] Qian Chen (陈潜),[4] Baoqing Meng (孟宝清),[4,a)] Chun Wang (王春),[2,a)] and Baolin Tian (田保林)[4,5]

AFFILIATIONS

[1]University of Chinese Academy of Sciences, Beijing 101408, China
[2]Institute of Mechanics, Chinese Academic of Sciences, Beijing 100190, China
[3]Graduate School of Chinese Academy of Engineering Physics, Beijing 100088, China
[4]Institute of Applied Physics and Computational Mathematics, Beijing 100094, China
[5]Center for Applied Physics and Technology, Peking University, Beijing 100871, China

[a)]**Authors to whom correspondence should be addressed:** mengbaoqing92@foxmail.com and wangchun@imech.ac.cn

ABSTRACT

Multiphase Richtmyer–Meshkov instability (RMI) widely exists in nature and engineering applications, such as in supernova explosions, inertial confinement fusion, particle imaging velocimetry measurements, and supersonic combustion. Few studies on the effects of heat transfer on the mix zone width have been conducted, and those that do exist are limited to dilute gas–particle flow. To address this research gap, the effects of dense particle heat transfer in a multiphase RMI flow were investigated in this study, and a dimensionless variable that integrates the particle volume fraction and particle parameters was derived for the first time. The results indicate that the effects of dense particle heat transfer cannot be neglected because the volume fraction increases by over three orders of magnitude compared to those in previous studies. Subsequently, numerical studies using the improved compressible multiphase particle-in-cell method were conducted to investigate the effects of heat transfer on the mix zone width. A detailed wave system structure and quantitative budget analyses were performed to investigate the inherent flow characteristics. The heat transfer effect was found to influence the fluid velocity by changing the fluid pressure gradient, thereby reducing the velocity and growth rate of the mix zone. With a Mach number of 2 and a 10% particle volume fraction, the heat transfer reduced the mix zone width by approximately 22%. In addition, simulations with different particle volume fractions and temperature self-similarity demonstrated the correctness and validity of the dimensionless heat transfer time, which is beneficial for predicting the effects of dense particle heat transfer.

I. INTRODUCTION

Richtmyer–Meshkov instability (RMI) is an instability phenomenon caused by shock waves passing through the interface between two different fluids.[1] In the initial stage of instability development, slight disturbances increase with time; then, "bubble" and "spike" structures occur.[2] The bubble is defined as the region where the lighter fluid penetrates into the heavier fluid, and similarly, the spike is the region where the heavier fluid penetrates into the lighter fluid. The distance between the outer edge of the bubble and the outer edge of the spike is called the mix zone width, which is the main interest in RMI research.

RMI widely exists in nature and engineering applications,[3–7] such as in supernova (SN) explosions,[8] inertial confinement fusion (ICF),[9] particle imaging velocimetry (PIV) measurement,[10] and supersonic combustion.[11–13] These RMI phenomena are often accompanied by the distribution of particle phases, which is not considered in traditional single-phase RMI. Multiphase RMI is closer to the actual situation than single-phase RMI, and its study is more meaningful. In an SN explosion, the shock wave generated by the outward projection of matter passes through the interface between materials of different densities, which induces RMI and then affects the life evolution of the star.[8] In ICF, the RMI triggers turbulent mixing between the fuel and ablative layer in the capsule, which can further affect the compression and formation of the central hot spot.[9] In RMI experiments, the PIV measurement uses the particles as passive tracer particles in the gas

phase, and the tracer effect is related to the ability of the particles to track the flow.[10] In supersonic combustion, the shock wave interacts with the interface of the fuel and oxidant to accelerate the mixing of the fuel and oxidant, which is beneficial for the combustion process.[11,12,14]

Multiphase RMI refers to the instability caused by the instantaneous acceleration of the interface of two particle-containing fluids of different densities caused by the passage of a shock wave. Unlike shock-driven granular instability, which focuses on particle dynamics, our study of multiphase RMI focuses on the mixing of gases. The mix zone width growth rate represents turbulent mixing between two different fluids. The theoretical and experimental research on pure gas-phase RMI has been relatively complete;[15–17] therefore, this paper will not elaborate much on this topic. Instead, the literature survey herein mainly focuses on research on the multiphase RMI theory and numerical simulation.

Research on multiphase RMI can be divided into two main categories. Studies in the first category involve modeling of the mix zone, and those in the second category explore the parameters affecting the mix zone width. Both research areas focus on the variation of the mix zone width. The research on mix zone modeling aims to provide an analytical expression of its growth rate, where the key variables are the particle volume fraction α_p and Stokes number St. α_p is used to determine whether the gas–particle flow is dilute gas–particle flow ($0 < \alpha_p < 0.01$), dense gas–particle flow ($0.01 < \alpha_p < \alpha_{p,packed}$), or granular flow ($\alpha_p > \alpha_{p,packed}$), as proposed by Zhang *et al.*[18] St is defined as the ratio of the response time of the particles to the characteristic time of the flow. For the multiphase RMI of dilute gas–particle flow, as early as 1961, Saffman provided an equation for the motion of gas carrying small dust particles.[19] In 2010, Ukai followed the method of Saffman to deduce the linear growth rate of RMI with small St and gave the multiphase Atwood number to measure the density gradient at the interface.[2] In 2019, the conclusions obtained for dilute gas–particle flow were extended to dense flow, large St, and the nonlinear stage, which strengthened the influence of the particle phase.[20–22] The multiphase RMI problem has a large parameter space, which demonstrates the complexity and diversity of this problem. In recent years, the rapid development of computational fluid dynamics has been inseparable from the realization of a more precise simulation of multiphase RMI. In addition to modeling to verify the results of the above theoretical studies, many targeted computational simulation studies have been performed. McFarland *et al.* focused on the effects of the gas–particle coupling, incident shock intensity, particle size, effective density difference, and particle relaxation time on multiphase RMI, emphasizing the importance of multiple coupling.[23] In addition, the re-shock process,[24,25] evaporation and breakup effects,[26,27] scale effect, electric field force,[28] and interaction force[29] in the multiphase RMI problem have been explored to varying degrees. Thus, the problem of multiphase RMI is complex and involves many physical phenomena.

Although the existing studies have explored the effects of many physical phenomena, the effect of interphase heat transfer is often neglected in dilute gas–particle flows.[24,30] The focus of the few articles that mention heat transfer effects can be divided into two categories. One is the difference between whether heat transfer is considered and the other is the comprehensive influence of heat transfer and evaporation on the mix zone.[23,26,27] Regarding heat transfer, little relevant research has been conducted, and this topic only appears in the work of McFarland *et al.*[23] These scholars conducted a numerical simulation analysis of the energy coupling caused by dilute particle heat transfer in a multiphase RMI problem. They pointed out that even for small particles with volume fractions of 0.014%–0.036%, the multiphase coupling effect is very important. Owing to the consideration of the heat transfer between the gas and particles, the particles have a cooling effect on the gas. These coupling effects can cause large deviations in the fluid temperature from the approximation obtained by the dusty gas model, particularly by up to 20% at higher shock strengths. Furthermore, two-way energy coupling increases the density of the carrier gas through the particle cooling effect, driving greater vorticity deposition. Through this approach, even small particles can generate additional circulation dissipation later. Moreover, heat transfer and evaporation are often considered together in multiphase RMI problems to explore their contributions to mix zone growth. Goossens *et al.* proposed a model of droplet evaporation caused by a shock wave propagating in fog.[27] The model was based on the existence of a quasi-steady wet-bulb state of the droplet during evaporation. The authors showed that for moderate impact strengths and droplet radii in the range of 1–5 μm, the major part of the evaporation process is governed by the balance between heat conduction and vapor diffusion. They further obtained an implicit analytical expression for the droplet evaporation time. Duke-Walker *et al.* also used the interphase heat transfer term in their study on evaporation and breakup.[26] Their research showed that large-scale hydrodynamic instability enhanced evaporation and droplet breakup significantly increased the strength of the instability and rate of droplet evaporation. Because few studies related to heat transfer in multiphase RMI exist, the above research is particularly important. These investigations have contributed to the exploration of heat transfer effects; however, some deficiencies remain. First, these studies have been based on dilute gas–particle flow, which is the main reason that the heat transfer effect has not been obvious in the previous studies. Second, the heat transfer effect has often been discussed together with the evaporation effect, preventing the independent influence and mechanism of heat transfer from being accurately analyzed.

To help fill the gaps in the existing research, the purposes of this study were to explore the influence of dense phase heat transfer on the fluid mix zone in the multiphase RMI problem and to determine the mechanism of the heat transfer effect, using a combination of theoretical analysis and numerical simulations. The compressible multiphase particle-in-cell (CMP-PIC) model[31,32] was improved by integrating the heat transfer model. This method can simulate all pattern flows from dilute to dense and granular flows, is more suitable for multiphase RMI simulations than previous approaches, and can provide more accurate flow details and particle properties. The remainder of this paper is organized as follows: Sec. II introduces the governing equations of the particle and gas phases under the Eulerian–Lagrangian framework. Based on this model, a heat transfer model and related coupling algorithms were added to simulate the interphase heat transfer effect in gas–particle flow. Section III provides a dimensionless number considering the particle volume fraction, obtained by deriving the fluid energy equation under the Lagrangian framework, to describe the effects of particle heat transfer on the fluid quantitatively. Section IV introduces the computational domain and the parameter settings of the simulation. Based on the numerical results, it illustrates the evolution of the location and width of the mix zone and describes the changes in various physical quantities in the process through wave system analysis. Section V discusses the influence chain of the heat transfer causing the velocity change in the mix zone through budget analysis and reveals the

mechanism of the heat transfer effect according to the momentum and energy equations. Section VI describes the use of numerical simulations to demonstrate the correctness and validity of the dimensionless relaxation time for heat transfer, considering several cases constructed to investigate the effects of the particle volume fraction and temperature self-similarity. Finally, the conclusions drawn from this study are presented in Sec. VII.

II. CMP-PIC MODEL AND IMPROVEMENT

This section presents the governing equations for the particle and gas phases based on the Eulerian–Lagrangian framework. The original CMP-PIC model ignores the effect of interphase heat transfer. In this study, the original model was improved to simulate the interphase heat transfer effect in the particle flow. Particles or parcels were tracked in the Lagrangian framework (in this study, the parcels were the same as the particles), and the gas equations were discretized in the Eulerian framework. The coupling algorithm required by the heat transfer module is then presented.

A. Particle equations

The particles were tracked in the Lagrangian coordinate system, which conforms to the dynamic properties of the particles themselves and makes the transitions of the particle phase properties natural under different volume fractions. Particles with similar properties were packaged, and the calculation was performed on coarse parcels to reduce the amount of calculation. The original CMP-PIC method includes the following particle position and momentum equations:

$$\frac{d\boldsymbol{x}_{p,i}}{dt} = \boldsymbol{v}_{p,i}, \tag{1}$$

$$\rho_{p,i}\frac{d\boldsymbol{v}_{p,i}}{dt} = \frac{\kappa_{p,i}}{V_{p,i}}(\overline{\boldsymbol{u}}_f - \boldsymbol{v}_{p,i}) - \nabla P_f - \rho_{p,i}\boldsymbol{A}_{p,i}, \tag{2}$$

$$\boldsymbol{A}_{p,i} = \frac{1}{m_{p,i}}\sum_j \boldsymbol{F}_{ij}, \tag{3}$$

where the subscript p corresponds to the particle phase, the subscript f corresponds to the gas phase, the subscript i is the parcel index, $\boldsymbol{x}_{p,i}$ is the position vector of parcel i, $\boldsymbol{v}_{p,i}$ is the velocity vector of parcel i, $\rho_{p,i}$ is the phase density of parcel i, $V_{p,i}$ is the volume of parcel i, $\kappa_{p,i}$ is the resistance coefficient between parcel i and the gas, $\overline{\boldsymbol{u}}_f$ is the average gas phase velocity vector in the cell, P_f is the gas phase pressure, $\boldsymbol{A}_{p,i}$ represents the collision term, and $m_{p,i}$ is the mass of parcel i.

For similar RMI problems, three force models exist in the particle momentum equation as source terms, namely, the drag force, pressure gradient force, and collision force models, which have been introduced in previous studies.[20] For comparison with the theoretical formula, the drag model that we adopted was the Stokes drag law, which was also assumed in previous research.[2,20,21] The expression for κ is $\kappa_p = 6\pi r_p \mu_f$, where r_p is the radius of the particle and μ_f is the gasdynamic viscosity. The collision force can be obtained using the discrete element method,[33] as shown in Eq. (3), where F_{ij} is the collision force between parcels i and j, which is equivalent to the effects of the spring-dashpot.

Before discussing the energy equation of the particles, we provide some basic assumptions. We typically assume that the temperature of a particle packet is uniform and equal to the temperature of the individual physical particles within it. Heat conduction inside individual particles is much faster than particle–fluid conduction.[34,35] In addition, the Biot number Bi is usually introduced in the literature to quantify the heat conduction inside the particle and that between the particle and fluid[36] and is defined as

$$Bi = \frac{Hr_p}{k_p}, \tag{4}$$

where H is the heat transfer coefficient, r_p is the radius of the particle, and k_p is the thermal conductivity of the particle. If the Biot number is much smaller than one, the heat conduction process inside the particle can be ignored, and the heat conduction process is considered to be completed instantaneously. In the usual simulation example, the heat transfer coefficient is approximately 0.1–1 mW/(m^2 K), the particle radius is approximately 0.01–0.1 mm, the particle thermal conductivity is approximately 0.1–1 W/(m K), and the Biot number is approximately 10^{-6}–10^{-9}, proving that the isothermal assumption is reasonable.

To explore the influence of the heat transfer effect, we added an interphase heat transfer model based on the original CMP-PIC model. In the particle energy equation, the energy source term mainly consists of the heat conduction between the particles and the gas. Because the particle collision time was extremely short, we ignored the heat conduction between the particles. In addition, we ignored the thermal radiation. Based on the particle equations presented by Crowe *et al.*,[37] we obtained the energy equation of the particles as follows:

$$m_{p,i}C_{par,i}\frac{dT_{p,i}}{dt} = \frac{m_{p,i}}{M_{p,i}}H\left(\overline{T}_f - T_{p,i}\right), \tag{5}$$

$$H = Nu\pi d_{p,i}k_f, \tag{6}$$

$$Nu = 2 + 0.6Re_r^{1/2}Pr^{1/3}, \tag{7}$$

$$Re_r = \frac{\rho_f d_p|\overline{\boldsymbol{u}}_f - \boldsymbol{v}_p|}{\mu_f}, \tag{8}$$

$$Pr = \frac{\mu_f Cp_f}{k_f}, \tag{9}$$

where $C_{par,i}$ is the specific heat capacity of parcel i, $T_{p,i}$ is the temperature of parcel i, $M_{p,i}$ is the mass of a single particle in parcel i, H is the heat transfer coefficient between parcel i and the gas, and $\overline{T}_f$ is the average gas-phase temperature in the cell.

The heat transfer between the particles and the gas is proportional to the temperature difference between the particles and the gas. The heat transfer coefficient is given by Eq. (5),[37] where Nu is the Nusselt number, d_p is the physical diameter of a single particle, and k_f is the thermal conductivity of the gas phase. The thermal conductivity changes with the incoming flow state. The forced convection effect of Ranz–Marshall yields the thermal conductivity equation in Eq. (6), which is related to the relative Reynolds number and Prandtl number of the flow,[38] whose expressions are given in Eqs. (7) and (8), respectively.

B. Gas phase equations

The gas phase equations were built on the Eulerian frame using a five-equation model of compressible flow, which includes the mass equation, momentum equation, energy equation, gas interface capture

equation, and gas–liquid fraction relationship. Viscous effects and gravity were ignored. Compared with the original CMP-PIC control equations, the energy coupling due to the interphase heat transfer appears as a source term on the right-hand side of the energy equation. The detailed forms of the equations are as follows:

$$\frac{\partial \boldsymbol{U}}{\partial t}+\frac{\partial \boldsymbol{F}}{\partial x}+\frac{\partial \boldsymbol{G}}{\partial y}=\boldsymbol{D}, \tag{10}$$

$$\boldsymbol{U}=\begin{pmatrix}\alpha_f\rho_f\\ \alpha_f\rho_f u_{fx}\\ \alpha_f\rho_f u_{fy}\\ \alpha_f\rho_f E_f\end{pmatrix}, \tag{10a}$$

$$\boldsymbol{F}=\begin{pmatrix}\alpha_f\rho_f u_{fx}\\ \alpha_f\rho_f u_{fx}u_{fx}+\alpha_f P_f\\ \alpha_f\rho_f u_{fy}u_{fx}\\ \alpha_f\rho_f E_f u_{fx}+\alpha_f P_f u_{fx}\end{pmatrix}, \tag{10b}$$

$$\boldsymbol{G}=\begin{pmatrix}\alpha_f\rho_f u_{fy}\\ \alpha_f\rho_f u_{fx}u_{fy}\\ \alpha_f\rho_f u_{fy}u_{fy}+\alpha_f P_f\\ \alpha_f\rho_f E_f u_{fy}+\alpha_f P_f u_{fy}\end{pmatrix}, \tag{10c}$$

$$\boldsymbol{D}=\begin{pmatrix}0\\ -P_f\frac{\partial\alpha_p}{\partial x}-\frac{1}{V_{cell}}\sum_i\left\{\kappa_{p,i}(\overline{u}_{fx}-v_{px,i})\right\}\\ -P_f\frac{\partial\alpha_p}{\partial y}-\frac{1}{V_{cell}}\sum_i\left\{\kappa_{p,i}(\overline{u}_{fy}-v_{py,i})\right\}\\ -\left(P_f\frac{\partial\alpha_p}{\partial x}v_{px,i}+P_f\frac{\partial\alpha_p}{\partial y}v_{py,i}\right)-\frac{1}{V_{cell}}\sum_i \boldsymbol{v}_{p,i}\boldsymbol{F}_i-\frac{1}{V_{cell}}\sum_i Q_i\end{pmatrix}, \tag{10d}$$

$$\boldsymbol{F}_i=\kappa_{p,i}(\overline{\boldsymbol{u}}_f-\boldsymbol{v}_{p,i}), \tag{11}$$

$$Q_i=\frac{m_{p,i}}{M_{p,i}}H\left(\overline{T}_f-T_{p,i}\right), \tag{12}$$

$$\frac{\partial\beta_1}{\partial t}+u_{fx}\frac{\partial\beta_1}{\partial x}+u_{fy}\frac{\partial\beta_1}{\partial y}=0, \tag{13}$$

$$\alpha_f+\alpha_p=1, \tag{14}$$

where α_f represents the volume fraction of the gas phase (including gases 1 and 2); ρ_f represents the phase density of the gas phase; u_{fx} and u_{fy} are the velocities of the gas phase in the x- and y-directions, respectively; E_f is the total energy of the gas phase; P_f represents the pressure of the gas phase; α_p represents the volume fraction of particles; V_{cell} is the volume of the Eulerian cell; $\overline{u}_{fx}$ and $\overline{u}_{fy}$ are the average velocities of the gas phase at the particle position in the x- and y-directions, respectively; $v_{px,i}$ and $v_{py,i}$ are the velocities of the parcel in the x- and y-directions, respectively; $\boldsymbol{F}_i$ is the drag force vector between parcel i and the gas phase; Q_i is the heat conduction between parcel i and the gas phase; and β_1 is the volume fraction of gas 1 in the whole gas phase.

The right-hand side of the gas momentum equation represents the momentum source term of the particles. It involves the nozzling and drag force terms, which were introduced in a previous study.[20] The right-hand side of the gas energy equation represents the energy source terms, which are the nozzling work, drag work, and heat conduction terms, as given in Eqs. (11) and (12). In addition, Eq. (13) is a gas interface capture equation used to capture the interface between two immiscible gases. It is especially important in problems involving material interfaces, such as RMI. The sum of the volume fractions of the gas and particle phases should be equal to 1, as shown in Eq. (14). The numerical simulations in this study were based on the governing equations above.

C. CMP-PIC and heat transfer algorithm

For our multiphase flow model, we implemented a simulation method based on the CMP-PIC approach. For the gas phase, the third-order Runge–Kutta method was applied for the time integration. The total variation diminishing[39] scheme was used to reconstruct the primary flow variables. A Riemann solver proposed by Harten *et al.*[40] was applied to obtain the intercell fluxes. For the particle phases, particles with similar physical properties were packed into a parcel. The collisions between the parcels were calculated using the soft sphere model. This calculation method can facilitate the calculation of coupling items and significantly reduce the amount of calculation required in large particle cloud simulations.

To calculate the heat transfer terms, heat was exchanged between the particles and gases through source terms, using the specific method shown in Fig. 1. We interpolated the gas-phase physical quantities (such as α_f, ρ_f, u_f, and T_f) on the grid at the Lagrangian points where the parcels are located by weight functions, calculated the interphase heat transfer at these positions, and then reassigned these coupling terms to the cell around the parcels by weight functions. Thus, heat was transferred from one system to another, providing two-way coupling between the particles and the gas.

For the verification that the original CMP-PIC method is suitable for large St and dense flow conditions, refer to the previous literature.[20,21,31,41] To verify the correctness, validity, and grid independence of the new model with added heat transfer, we verified its calculation results. The verification results are presented in the Appendixes. Appendix A contains the verification of a simple case of the heat transfer module and the comparison with theoretical solutions, and Appendix B contains the verification of grid independence.

III. HEAT TRANSFER RELAXATION TIME IN DENSE PARTICLE-GAS FLOW

The influence of heat transfer is mainly reflected in the energy equation of the fluid, which is also the main factor affecting the velocity in the mix zone; therefore, the energy equation must be analyzed in detail. We explored the difference in fluid temperature between dense

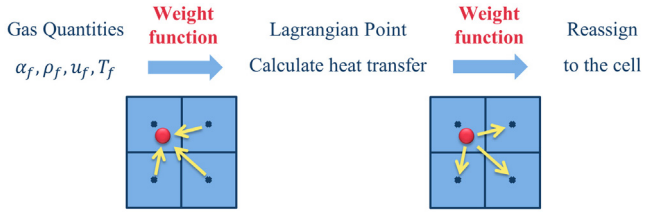

FIG. 1. Flowchart of coupled heat transfer between gas and particles.

and dilute flows through a theoretical analysis. Combined with the energy equation, we derived a dimensionless number considering the volume fraction to describe the effect of particle heat transfer on the fluid quantitatively.

To track the temperature change of a specific fluid microelement, the energy equation must be converted from the Eulerian frame into the Lagrangian frame. We assumed that the particles were evenly distributed and that parameters such as the particle density, diameter, and shape were the same. Then, we derived the energy equation of the gas phase in the x-direction under the Lagrangian framework as

$$\alpha_f \rho_f C_v \frac{DT_f}{Dt} = -P_f\left(\frac{\partial \alpha_f u_{fx}}{\partial x} + \frac{\partial \alpha_p v_{p,x}}{\partial x}\right) - \frac{\alpha_p}{V_p}\kappa(u_{fx} - v_{px})^2 - \frac{\alpha_p}{V_p}H(T_f - T_p). \tag{15}$$

The left-hand side of the energy equation is the time derivative term of the fluid temperature in the control volume, and the right-hand side consists of the nozzling, drag work, and heat transfer terms. The heat transfer term reduces the temperature of the gas phase. According to the gas state equation, we can further infer that the gas phase pressure will decrease accordingly, which is also the basic premise of the heat transfer mechanism.

In the energy equation under the Lagrangian framework, we defined the ratio of the heat transfer and nozzle terms as $\alpha_{heat\&nozzling}$ and the ratio of the heat transfer and drag work terms as $\alpha_{heat\&drag}$. Considering large St, the particle velocity is always zero and the particle volume fraction remains constant throughout the process. Therefore, these ratios can be expressed as

$$\alpha_{heat\&nozzling} = \frac{\frac{\alpha_p}{V_p}H(T_f - T_p)}{P_f\left(\frac{\partial \alpha_f u_{fx}}{\partial x} + \frac{\partial \alpha_p v_{p,x}}{\partial x}\right)} = \frac{\alpha_p H(T_f - T_p)}{\alpha_f V_p P_f \frac{\partial u_{fx}}{\partial x}}, \tag{16}$$

$$\alpha_{heat\&drag} = \frac{\frac{\alpha_p}{V_p}H(T_f - T_p)}{\frac{\alpha_p}{V_p}\kappa(u_{fx} - v_{px})^2} = NuPr^{-1}\frac{C_p(T_f - T_p)}{3(u_{fx} - v_{px})^2}. \tag{17}$$

For the usual example of dense gas–particle flow with large St, $\alpha_{heat\&nozzling}$ and $\alpha_{heat\&drag}$ are approximately 1–10^3, which means that $\alpha_{heat\&nozzling} \gg 1$ and $\alpha_{heat\&drag} \gg 1$ are constant. This relationship is due to the tiny particle radius, velocity gradient, and drag coefficient, which were also verified in the subsequent numerical simulations. Ignoring the nozzle and drag work terms, Eq. (15) can be simplified to

$$\alpha_f \rho_f C_v \frac{DT_f}{Dt} \approx -\frac{\alpha_p}{V_p}H(T_f - T_p). \tag{18}$$

Owing to the high specific heat capacity of the particles, their temperature remains constant throughout the process; that is, $T_p = T_{p0}$. Let t' be the time after the shock wave passes through the interface. When the shock wave passes through the interface ($t' = 0$), the gas-phase temperature is the post-shock wave temperature, T_{shock}. Integrating Eq. (18) yields

$$T_f = (T_{shock} - T_{p0})e^{-\frac{\alpha_p H}{\alpha_f \rho_f C_v V_p}t'} + T_{p0}. \tag{19}$$

Thus, we obtained the relaxation time for heat transfer, $t_T = \frac{\alpha_f \rho_f C_v V_p}{\alpha_p H}$. Physically, after the temperature relaxation time t_T, the temperature difference between the fluid and particles decreases to e^{-1} of the original value. Taking the impact propagation time in fluid kinematics as the characteristic time, $t_c = \frac{L_x}{U_{shock}}$, where L_x is the length in the flow direction, the dimensionless heat transfer relaxation time is

$$\tau_T = \frac{t_T}{t_c} = \frac{\alpha_f}{\alpha_p}\frac{\rho_f C_v V_p U_{shock}}{L_x H}. \tag{20}$$

We can use the dimensionless number of heat transfer relaxation times as the basis for judging the influence of the heat transfer effect in multiphase RMI. When $\tau_T \gg 1$, the heat transfer relaxation time is much longer than the flow time, and the heat transfer can be ignored. When $\tau_T \sim 1$, the heat transfer relaxation time is close to the flow time, and the heat transfer effect needs to be considered in detail. Finally, when $\tau_T \ll 1$, the heat transfer relaxation time is much shorter than the flow time, which means that the heat balance is completed quickly after contacting the particles, and the calculation is based on the physical quantity after heat balance.

From the dimensionless relaxation time of heat transfer, we know that the smaller the volume fraction of particles, the longer the relaxation time. Similarly, the larger the volume fraction of particles, the shorter the relaxation time. Obviously, for the dilute gas–particle flows considered in previous studies, $\alpha_p \to 0$; then, $\tau_T \to \infty$. For example, when $\alpha_p = 0.01\%$, as is often the case in dilute gas–particle flow,[23,26] t_T is approximately 6.8 s, t_c is approximately 0.3 ms, and τ_T is approximately 2.3×10^4, which means that the temperature relaxation time is much longer than the time required for shock wave movement, so the effect of heat transfer is very small and can be ignored. This characteristic also explains why previous scholars believed that the heat transfer effect does not have a significant effect on the development of instability. However, when the volume fraction of the particles is sufficiently large, significant heat transfer occurs within the characteristic time of the flow. For example, when $\alpha_p = 10\%$, t_T is approximately 0.6 ms, t_c is approximately 0.3 ms, and τ_T is approximately 2. Therefore, we cannot continue to assume that the effect of heat transfer is negligible. For dense gas–particle flow or even granular flow, the heat transfer effect needs to be considered seriously.

The heat transfer relaxation time is the time required for the temperature of the fluid to decrease to a certain degree. This dimensionless number characterizes the heat transfer effect. In other words, for two cases with the same dimensionless heat transfer relaxation time, the temperature changes also have a certain similarity. We call it the "temperature self-similarity," which is convenient for the prediction of related calculation cases later.

IV. MIX ZONE GROWTH SIMULATION AND ANALYSIS

From the above analysis, we know that when discussing dense gas–particle flow, the effect of heat transfer is significant. This section presents concrete examples to describe the effects of heat transfer on the development of the mix zone. First, basic information such as the computational domain and parameter settings in the simulation is introduced. Then, based on the numerical results, we illustrate the evolution of the location and width of the mix zone and describe the physical changes that occur in the process through wave system analysis. We also explained the influences and reasons of heat transfer on vorticity generation.

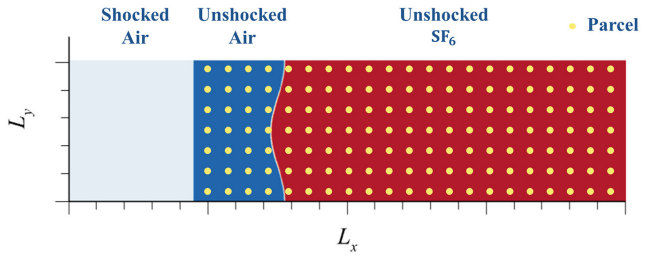

FIG. 2. Visualized computational domain. The small circles in the domains of unshocked air and SF_6 represent the uniformly distributed particle cloud.

A. Simulation domain and initial conditions

Interface multiphase RMI was analyzed in two-dimensional single-mode air/SF_6, where the particles were uniformly distributed; this situation has often been employed in other studies as well.[2,20,24] The computational domain used in this study is illustrated in Fig. 2. The length in the flow direction is $L_x = 80$ mm, and the length in the transverse direction is $L_y = 10$ mm. L_s is the location of the shock wave at the initial moment, L_i is the location of the air/SF_6 interface at the initial moment, a_0 is the amplitude of the interface at the initial moment, λ is the wavelength of the interface at the initial moment, P_0 is the pressure of the unshocked fluid at the initial moment, T_0 is the temperature of the unshocked fluid at the initial moment, Ma is the shock Mach number of the moving shock, L_p is the location of the uniform particle distribution at the initial moment, and α_{p0} is the particle volume fraction at the initial moment. The values of these physical quantities are listed in Table I.

The interface perturbation mode is given by Eq. (21). The initial perturbation amplitude $a_0 = 0.5$ mm, and the perturbation wavelength $\lambda = 10$ mm. The volume fraction of air, β_1, was smoothed around the interface using an error function, as was also done in another study.[42] In the subsequent calculations, the selected $\beta_1 = 50\%$ position was considered as the interface position between the air and SF_6. The left boundary was set as the inlet, the right boundary was set as the outlet, and the upper and lower sides of the computational domain were set as the periodic boundaries for the gas and particles

$$a(y) = a_0 \cos\left(\frac{2\pi}{\lambda} y\right). \tag{21}$$

As mentioned above, the Stokes number of particles is one of the key parameters in multiphase RMI research and can characterize the performance of particles, as shown in Eq. (22). τ_p is the relaxation time for the particles to be accelerated by drag. For RMI, we chose τ_p to be the ratio of the particle mass to the drag coefficient κ, as shown in Eq. (23). τ_f is the characteristic time of gas-phase flow. For RMI, we chose τ_f to be the ratio of the disturbance amplitude a to the post-impact interface velocity U_{shock}, as shown in Eq. (24). In this study, we designed a calculation case with large St to research the problem. Here, the response time of the particle is approximately 0.26 s, the characteristic time of the flow is approximately 10^{-6} s, and the Stokes number is approximately 260 000, so the particle remains stationary during the entire process

$$St = \frac{\tau_p}{\tau_f}, \tag{22}$$

$$\tau_p = \frac{\rho_p V_p}{6\pi r_p \mu}, \tag{23}$$

$$\tau_f = \frac{a}{U_{shock}}. \tag{24}$$

TABLE I. Computational domain parameters.

L_s (mm)	L_i (mm)	a_0 (mm)	λ (mm)	P_0 (kPa)	T_0 (K)
9	15	0.5	10	101	298
Ma	L_p (mm)	α_{p0}	ρ_p (kg/m^3)	d_p (mm)	C_{par} (J/kg K)
2.0	>10	10%	7800	0.1	4200

B. Comparison of mix zone growth

We first considered two sets of cases: the RMI case with heat transfer and the RMI case without heat transfer, which are referred to hereafter as "heat transfer system" and "non-heat transfer system," respectively. Within a given calculation time (0.2 ms), the change diagram of the volume fraction of air in the gas phase in the non-heat transfer system is as shown in Fig. 3. The interface in the figure represents the interface between the air and SF_6. The part where air intrudes into SF_6 is called a bubble, and the part where SF_6 intrudes into air is called a spike. The distance between the bubble and spike is the width of the mix zone. Figure 3(a) depicts the mix zone at the initial moment, and Fig. 3(b) shows the mix zone at 60 μs. The interface moves downstream, and the cosine mode remains, but the disturbance amplitude increases. Figure 3(c) illustrates the mix zone at 120 μs, where the interface moves further downstream, the overall pattern is no longer cosine, more obvious peaks and bubbles appear, and the width of the mix zone increases further. Finally, Fig. 3(d) depicts the mix zone at 180 μs, where the interface leaves the computational domain, the bubbles gradually become flat, and a more obvious vortex structure appears in the spike area.

We compared the interface position and shape of the heat transfer system and non-heat transfer system at 180 μs, as shown in Fig. 4. Figures 4(a) and 4(b) correspond to the non-heat transfer system and heat transfer system, respectively. The x-coordinate of the interface in the heat transfer system is smaller than that in the non-heat transfer system, indicating that the mix zone moves more slowly in the former case. The mix zone width in the heat transfer system is also shorter than that in the non-heat transfer system.

The evolutions of the spike and bubble boundaries in the mix zone over time are shown in Fig. 5, in which L_{spike} and L_{bubble} are the locations of the spike and bubble boundaries, respectively. The physical quantities with and without the subscript "heat" in the figure correspond to the heat transfer system and non-heat transfer system cases, respectively. These subscript rules also apply to the subsequent figures. Under the given conditions, both the spike and bubble boundaries of the mix zone increase with time. Compared with the non-heat transfer system, the start and end positions of the mix zone in the heat transfer system are reduced, and the gap between the two gradually increases with time. The distance between the start and end positions is the width of the mix zone, as shown in Fig. 6. The mix zone width in both

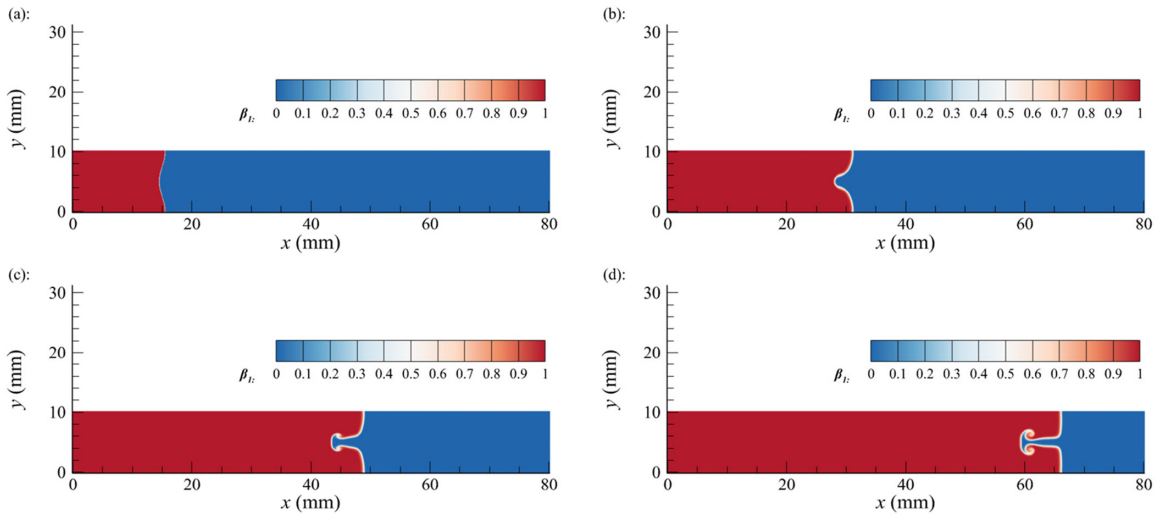

FIG. 3. Mix zone interface in the non-heat transfer system at (a) 0, (b) 60, (c) 120, and (d) 180 μs.

systems exhibits linear and nonlinear phases and generally shows an exponentially decreasing trend, which is consistent with the conclusions of previous research on large-*St* RMI.[21] Compared with the non-heat transfer system, the mix zone width in the heat transfer system is reduced by approximately 22%, the growth rate is slower, and the nonlinear stage occurs slightly earlier.

For general multiphase RMI problems, the width of the mix zone is primarily affected by the initial amplitude a_0^+, Atwood number At^+, Stokes number St, and mixing interface velocity U.[2,21] However, because the mixing interface is relatively close upstream, the shock wave passes through the mix zone at a very early stage (approximately 0.01 ms). At this time, the influence of the heat transfer is not obvious, and the physical quantities (a_0^+, ρ, U_{shock}) after the wave of the heat transfer system are not significantly different from those of the non-heat transfer system. However, the interphase heat transfer affects the fluid and particles behind the shock wave for a long time, and the influence on the mix zone is mainly caused by the changing fluid velocity in the mix zone.

C. Comparison of wave system structure analysis

To analyze the entire process in more detail, the distribution changes of various physical quantities in heat transfer and non-heat

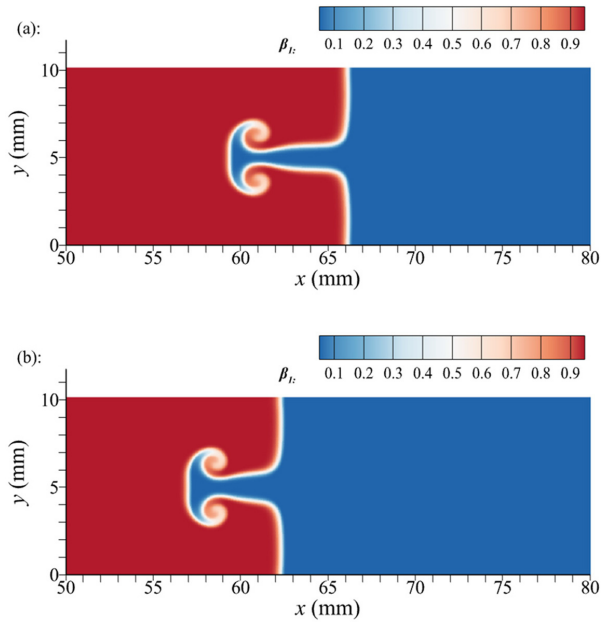

FIG. 4. Comparison of the position and shape of the interface at 180 μs in the (a) non-heat transfer system and (b) heat transfer system.

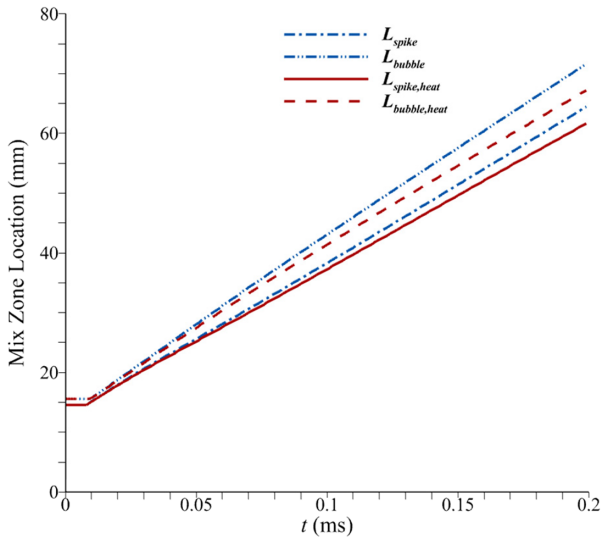

FIG. 5. Evolution of spike and bubble locations in the heat transfer and non-heat transfer systems.

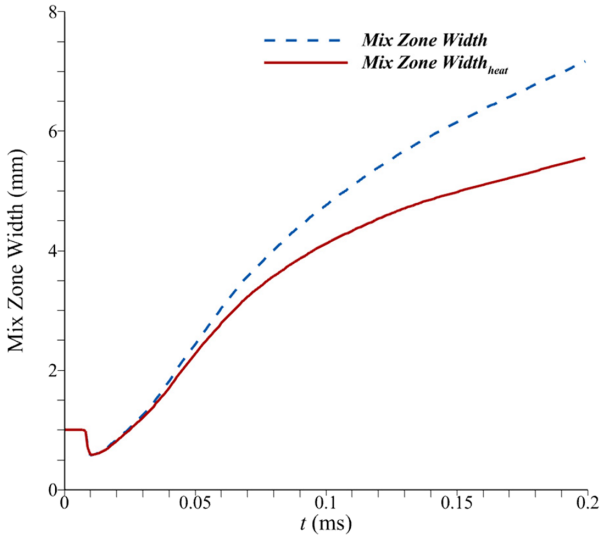

FIG. 6. Evolution of mix zone width in the heat transfer and non-heat transfer systems.

transfer systems must be explored to elucidate the reason for the velocity variation near the mix zone in both systems. At three typical moments (0, 25, and 75 μs), we took the average of each physical quantity in the lateral direction and made it dimensionless. The distribution in the flow direction is shown in Fig. 7. The dimensionless method is based on the corresponding physical quantities of air after the wave, for which Ma is 2. β_1 is the volume fraction of air in the gas phase, P_f^* is the dimensionless gas-phase pressure, u_x^* is the dimensionless gas-phase flow velocity, and T_f^* is the dimensionless average temperature of the gas phase.

At 0 μs, each physical quantity is a given value, and corresponding value jumps occur at the particle and SF_6 interfaces, as depicted in Fig. 7(a). At 25 μs, the shock wave passes through the interface and two reflected shock waves appear at the particle and SF_6 interface, whereas the right-going shock wave continues to move, as shown in Fig. 7(b). At 75 μs, the two reflected shock waves leave the particle area, and the right-going shock wave continues to move until it leaves the particle area, as illustrated in Fig. 7(c). The β_1 curve can be used as a representation of the position of the mix zone, which gradually moves to the right with time. The changes in pressure, flow velocity, and temperature are controlled by the above three shock waves, and the changes are the most severe near the right-going shock wave.

The physical quantities are compared between the heat transfer and non-heat transfer systems at 25 μs in Fig. 8. The distributions of the gas pressure and temperature are shown in Fig. 8(a). The interphase heat transfer most directly affects the gas-phase temperature in the particle-containing region and then affects the gas pressure. The temperature and pressure of the heat transfer system are lower than those of the non-heat transfer system in the particle-containing region passing by the right-hand shock wave.

The distributions of β_1 and the gas phase velocity in the heat transfer and non-heat transfer systems are presented in Fig. 8(b).

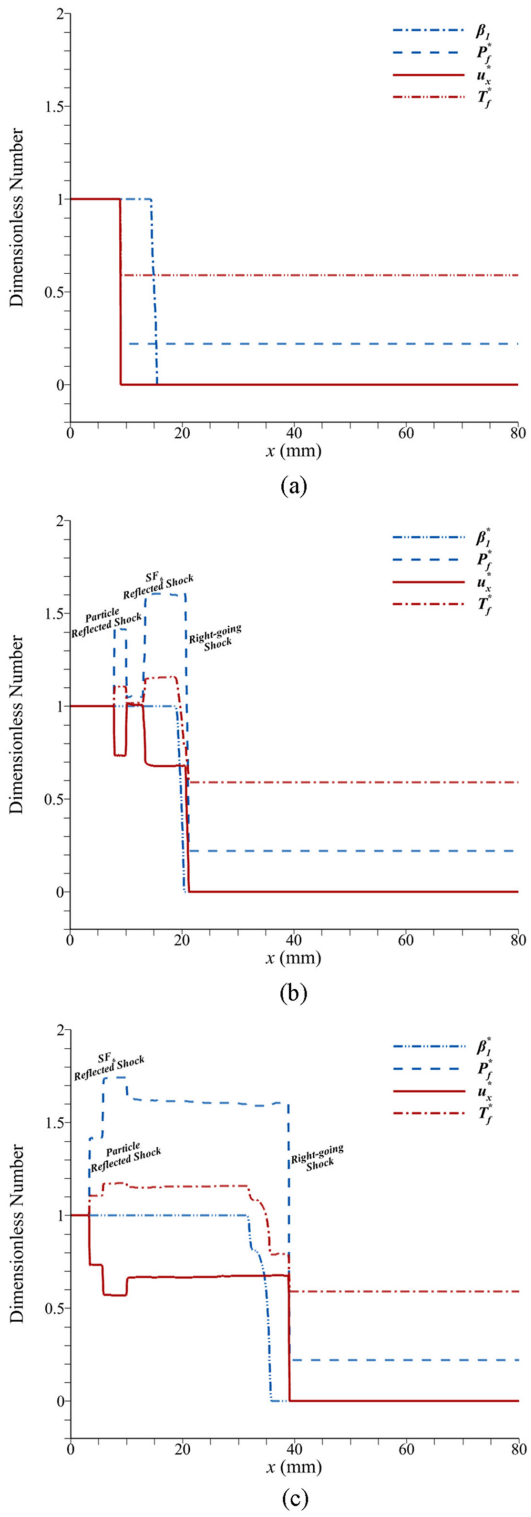

FIG. 7. Distribution diagram of dimensionless physical quantities in the non-heat transfer system at (a) 0, (b) 25, and (c) 75 μs. The dimensionless method is based on the corresponding physical quantities of air after the wave, where Ma is 2.

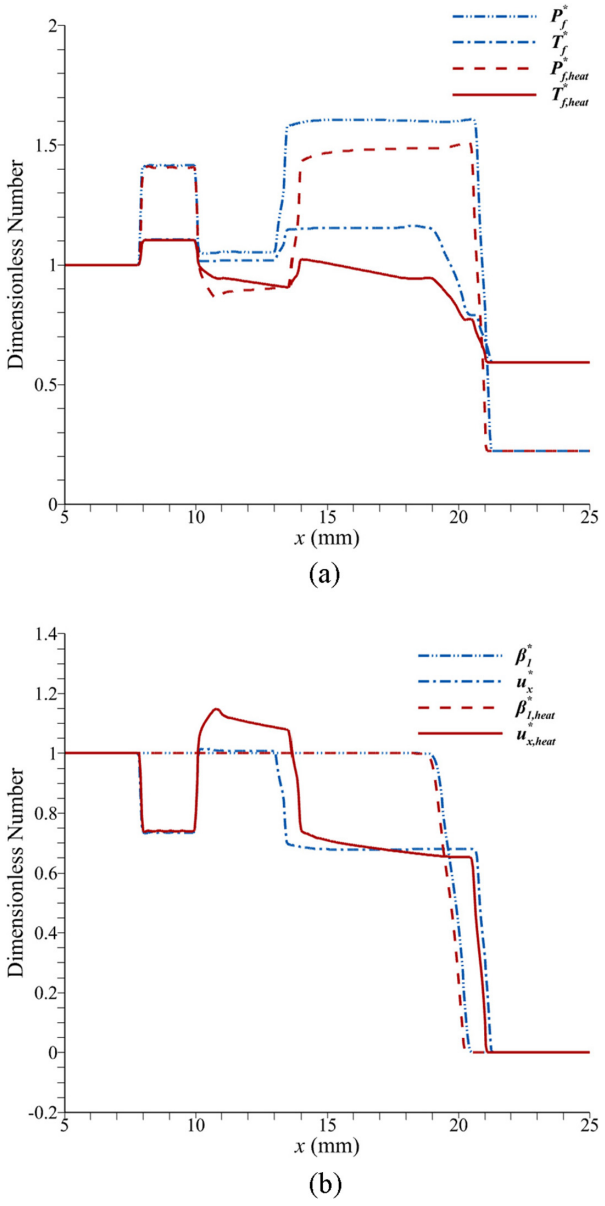

FIG. 8. Comparison diagram of physical quantity distributions in the heat transfer and non-heat transfer systems at 25 μs: (a) gas phase pressure and temperature and (b) β_1 and gas phase velocity.

The new pressure distribution of the heat transfer system causes the fluid velocity after the shock wave to exhibit a new distribution. In the heat transfer system, when the fluid enters the particle-containing region, the fluid velocity is relatively high because of the relatively large pressure gradient near the boundary of the particle-containing region. However, near the right-going shock wave, because the shock wave intensity of the heat transfer system is relatively low, the acceleration of the fluid is relatively small when the shock wave passes through. Therefore, the fluid velocity is relatively low after the right-going shock wave. Under these conditions, the position of the mix zone is closer to the right-going shock wave, and the fluid deceleration caused by the reduction in the right-going shock wave intensity and the influence of the nearby pressure gradient are dominant. The process of heat transfer affecting the fluid velocity is analyzed and summarized in Fig. 9.

Because of the unique gradient distribution of the fluid velocity in the heat transfer system, the velocity of the spike boundary in the mix zone is faster than that of the bubble boundary; therefore, the growth rate of the mix zone width (the difference between the velocities at the start and end positions) of the heat transfer system is slower than that of the non-heat transfer system.

The physical quantities in the heat transfer and non-heat transfer systems at 75 μs are compared in Fig. 10. The distributions of the gas pressure and temperature are shown in Fig. 10(a), and those of β_1 and the gas-phase velocity are provided in Fig. 10(b). The difference in the analysis results for 75 μs is more obvious than those in the results for 25 μs, especially in the distributions of fluid temperature, pressure, and flow velocity; however, the qualitative rules are consistent with those at 25 μs and thus are not repeated here.

Therefore, the heat transfer effect can make the mix zone move and grow more slowly. During this process, the decrease in the intensity of the right-going shock caused by interphase heat transfer is the main reason for the decrease in velocity.

D. Comparison of vorticity generation

The RMI develops as a result of vorticity deposition along the interface by the production of baroclinic torque. This process can be described using the compressible vorticity transport equation, which is commonly used in research on RMI problems.[43–46] Under the Lagrangian framework, the fluid vorticity equation is derived by taking the curl for the fluid momentum conservation equation,[30]

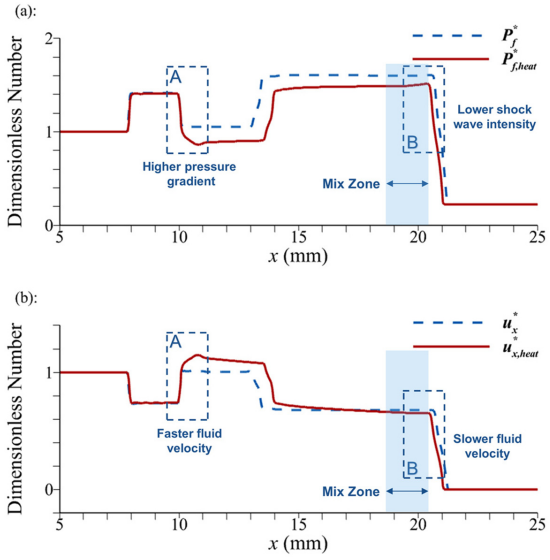

FIG. 9. Fluid velocity variation near particle-containing region and right-going shock wave in the heat transfer and non-heat transfer systems at 25 μs: (a) gas phase pressure and (b) gas phase velocity. Region A is near the boundary of the particle-containing region, and region B is near the right-going shock.

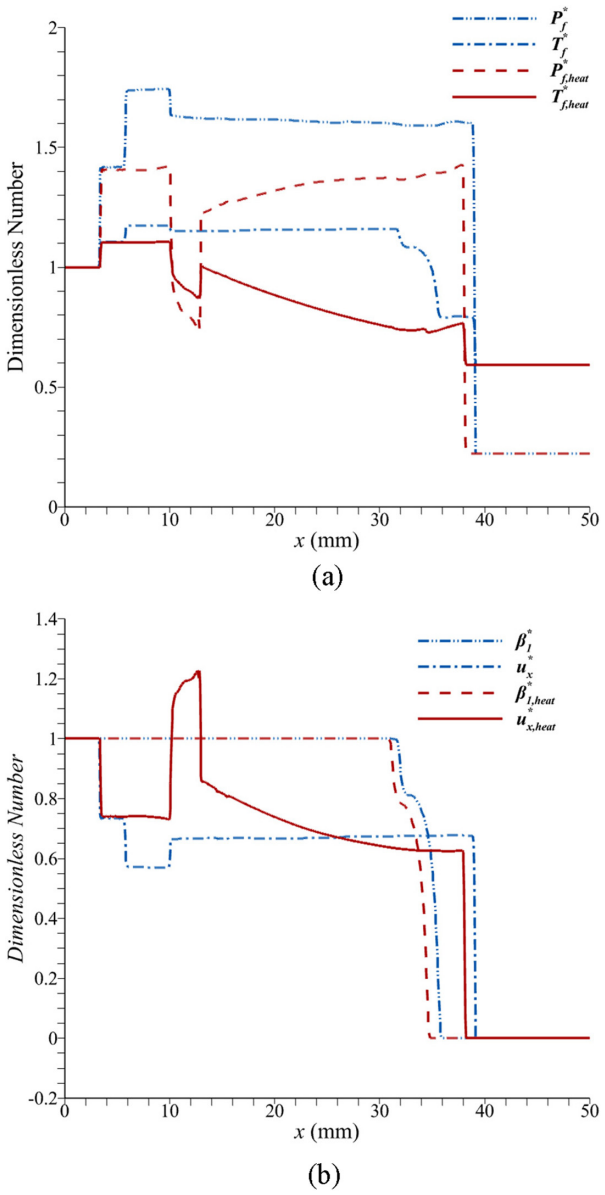

FIG. 10. Comparison of physical quantity distributions in the heat transfer and non-heat transfer systems at 75 μs: (a) gas phase pressure and temperature and (b) β_1 and gas phase velocity.

$$\frac{D\boldsymbol{\omega}}{Dt} = (\boldsymbol{\omega}\cdot\nabla)\boldsymbol{u_f} - \boldsymbol{\omega}(\nabla\cdot\boldsymbol{u_f}) + \left[\frac{1}{\rho_f^2}\nabla\rho_f\times\nabla P_f\right]_{baroclinic\ term} - \left[\nabla\times\left(\frac{\boldsymbol{f}}{\alpha_f\rho_f}\right)\right]_{multiphase\ term}, \quad (25)$$

where $\boldsymbol{\omega}$ is the fluid vorticity. $\boldsymbol{f} = \frac{\alpha_p}{V_p}\kappa(\boldsymbol{u_f} - \boldsymbol{v_p})$ is the momentum coupling term due to the drag force, where the identical particle assumption is also used here. The left-hand side of the equation is the material derivative of vorticity; the first two terms on the right-hand side represent the transport of vorticity through vortex stretching and dilatation, the third term represents the vorticity generated by the baroclinic moment due to the misalignment between the density gradient and the pressure gradient, and the fourth term is the additional vorticity generated in the multiphase flow, which is caused by the interphase momentum coupling term. It can be clearly seen from the multiphase term that as the particle volume fraction increases, the influence of the multiphase term on the vorticity increases gradually.

To explore the process of fluid vorticity generation and change, the fluid vorticity cloud maps of the heat transfer and non-heat transfer systems at typical moments (60, 120, and 180 μs) are shown in Fig. 11. With increasing time, the fluid vortices near the mix zone are gradually curled and deposited. The main difference in the vorticity distributions of the heat transfer and non-heat transfer systems remains in the x-direction position. In addition, the vorticity of the heat transfer system is lower than that of the non-heat transfer system due to the reduction in fluid velocity caused by the heat transfer effect. During the whole process, the baroclinic term is always greater than the multiphase term. Taking the cloud map at 180 μs as an example, the magnitude of the baroclinic term is 1×10^9, whereas the magnitude of the multiphase term is 1×10^8 near the mix zone, as shown in Fig. 12. In other words, the generation of fluid vorticity is still dominated by the baroclinic moment, and the multiphase term only produces a small amount of promotion/inhibition. Both the baroclinic term and the multiphase term are slightly smaller in the heat transfer system than those in the non-heat transfer system, due to the decrease in fluid pressure and the slight increase in fluid density.

Therefore, the heat transfer effect will slow down the vortex generation, and the baroclinic moment remains the main driver of vortex deposition.

V. MECHANISM OF EFFECT OF HEAT TRANSFER ON MIX ZONE VELOCITY

Knowing the distribution of each physical quantity in the entire process enables the exploration of the mechanisms of their effects on the velocity. Based on the numerical results, this section provides the reasons for the velocity variations caused by heat transfer based on the budget method and an analysis of the mechanism of the heat transfer effects according to the momentum and energy equations.

A. Comparison of mix zone velocity

To analyze the variations in the mix zone further, the velocity of the mix zone interface must be obtained. The mix zone interface is a theoretical concept that does not have a physical mass. Numerically, the position at which the volume fraction of air in the gas is 0.5 ($\beta_1 = 50\%$) is considered to correspond to the mix zone interface. We take microelements at the spike and bubble boundaries to represent the start and end positions of the interface in the flow direction, respectively, and take the velocities of the microelements at the spike and bubble as those of the interface start and end positions, respectively.

The fluid velocities at the spike and bubble boundaries are depicted in Fig. 13. During the entire process, the velocities at the start and end positions generally exhibit downward trends. Compared with the non-heat transfer system, the velocities of the start and end positions of the mix zone in the heat transfer system are lower, and the gap gradually increases with time.

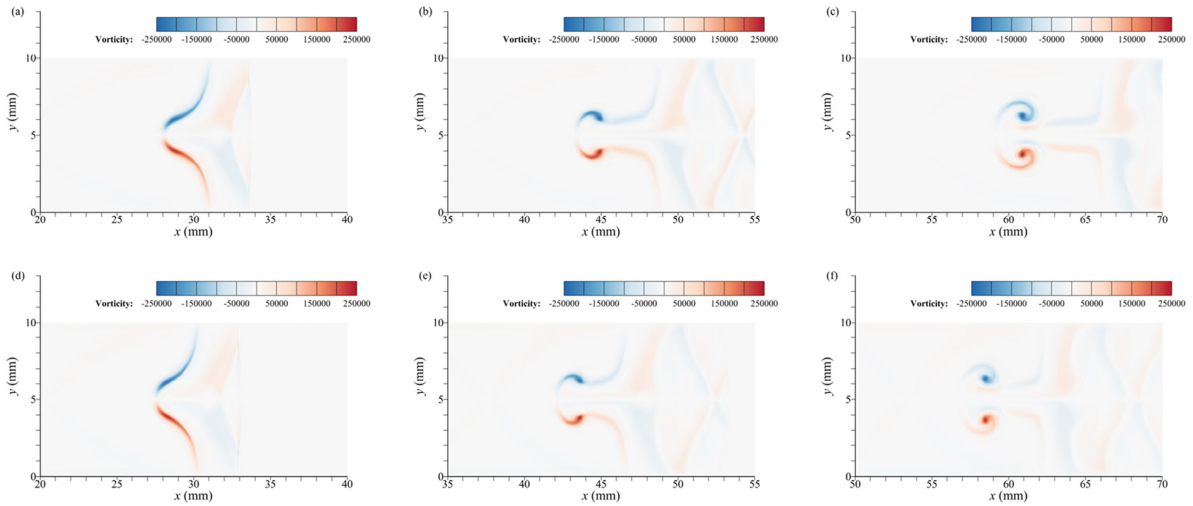

FIG. 11. Comparison of vorticity evolution between (a) 60, (b) 120, and (c) 180 μs in the heat transfer system and (d) 60, (e) 120, and (f) 180 μs in the non-heat transfer system.

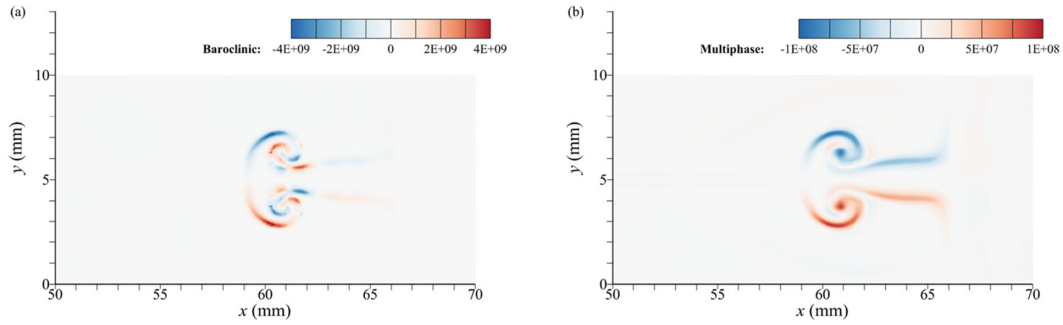

FIG. 12. Cloud maps of baroclinic and multiphase terms at 180 μs in the non-heat transfer system.

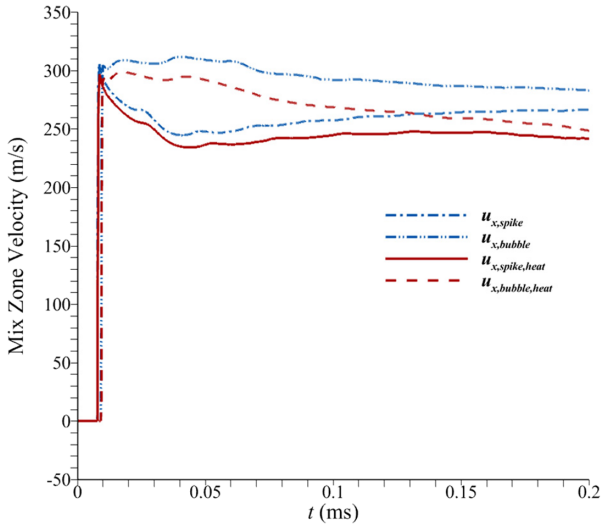

FIG. 13. Fluid velocities of spikes and bubbles in the heat transfer and non-heat transfer systems.

The difference between the fluid velocities at the spike and bubble boundaries is the growth rate of the mix zone width, as shown in Fig. 14. During the entire process, the growth rate of the mix zone width first increases and then decreases slowly. In the heat transfer system, because the initial velocity reduction at the spike and bubble is due to the reduction in the shock wave intensity, the velocity reduction is similar, so the growth rate of the mix zone width remains unchanged. However, in the subsequent process, the velocity of the bubble boundary decreases faster than that of the spike boundary; thus, the growth rate of the mix zone width also decreases.

Therefore, the heat transfer effect causes a decrease in the velocities of the mix zone spikes and bubbles. In addition, the velocity at the bubbles decreases faster than that at the spikes, so the mix zone width growth rate is reduced.

B. Budget analysis of heat transfer effects on mix zone velocity

Still using the assumption of identical particles, the momentum equation of the gas phase in the x-direction in the Lagrangian framework can be expressed as

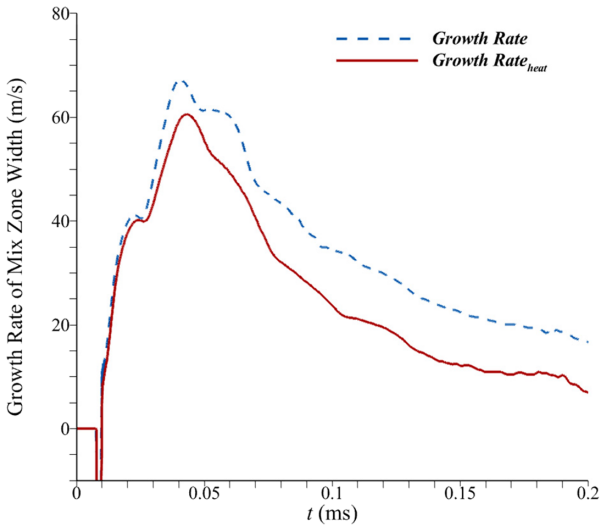

FIG. 14. Mix zone width growth rates in the heat transfer and non-heat transfer systems.

$$\alpha_f \rho_f \frac{Du_{fx}}{Dt} = -\alpha_f \frac{\partial P_f}{\partial x} - \frac{\alpha_p}{V_p} \kappa (u_{fx} - v_{px}). \tag{26}$$

The left-hand side of the momentum function in Eq. (26) is the time derivative term of the flow direction velocity of the fluid microelement, and the right-hand side of the equation consists of the pressure gradient and drag force terms. To extract the various factors that affect the velocity accurately and to judge the relative sizes of their effects to determine the main mechanism of heat transfer, an analysis method called "budget analysis" must be employed. Budget analysis is often used in turbulence research. It extracts the items in the equation independently and displays the relative size and change in different items by drawing their time-varying images. We took cell-sized control volumes at the spike and bubble as typical fluid microelements at the spike and bubble boundaries, respectively, in the budget analysis in this study.

Figure 15 depicts the pressure gradient and drag force terms in the momentum equation of the two fluid microelements at the start and end positions, which are expressed as $-\alpha_f \frac{\partial P_f}{\partial x}$ and $-\frac{\alpha_p}{V_p}\kappa(u_{fx} - v_{px})$, respectively. The pressure gradient term is much larger than the drag force term. Compared to the non-heat transfer system, the heat transfer system has different degrees of reduction and hysteresis in the pressure gradient term.

To see their effects more clearly, we integrated these two terms over time to explore their cumulative effects on fluid momentum, as shown in Fig. 16. Here, the integral of the drag term is always negative, and it decreases linearly with time. Meanwhile, the influence of the pressure gradient term on the fluid velocity is dominant, and its contribution to the momentum equation accounts for approximately 95%; therefore, the integrated curve is similar to the fluid velocity curve. Initially, the heat transfer system reduces the shock wave intensity and the pressure difference between before and after the shock wave owing to the cooling effect of the particles. Therefore, the velocity after the shock wave is lower in the heat transfer system than in the non-heat transfer system. Subsequently, the integral of the pressure gradient term of the heat transfer system is still significantly lower than that of the non-heat transfer system. As time progresses, the gap between the two gradually widens, which further illustrates that the influence of heat transfer decreases the pressure gradient term throughout the process and the deceleration effect becomes more significant.

Therefore, throughout the process, the pressure gradient has a much greater effect on the velocity than the drag force, and the heat transfer effect reduces the pressure gradient, causing the main deceleration effect on the fluid. The mechanism of the effect of the interphase heat transfer on the growth rate of the mix zone width is summarized in Fig. 17. Heat transfer affects the pressure gradient by reducing the temperature and pressure in the particle-containing region. Compared with the fluid downstream, the fluid upstream is affected by heat transfer for a longer time, and the temperature and pressure are lower, so the pressure gradient is larger, which determines the change in velocity and causes a more significant deceleration effect on the fluid. Near the mix zone, the velocities at the spike and bubble decrease. Because the

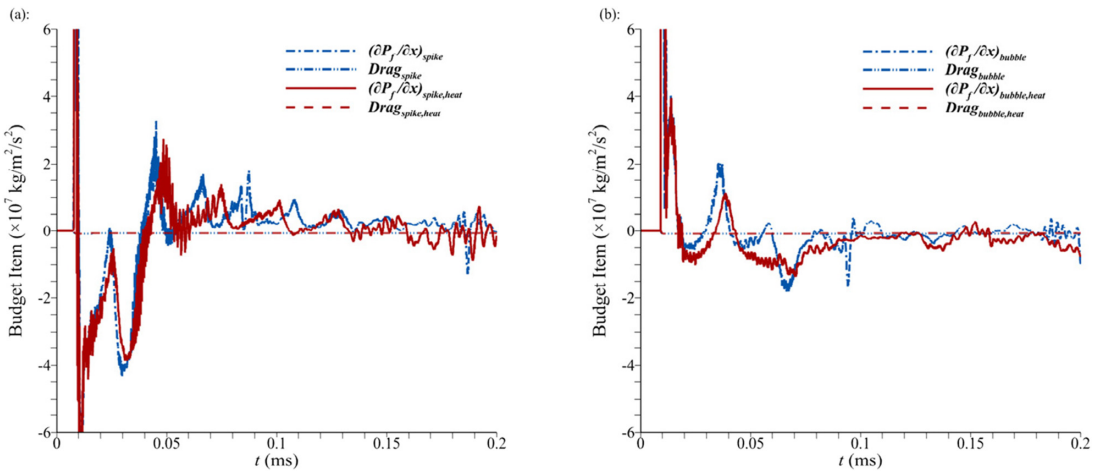

FIG. 15. Budget analysis results obtained using the momentum equations at the (a) spike and (b) bubble in the heat transfer and non-heat transfer systems.

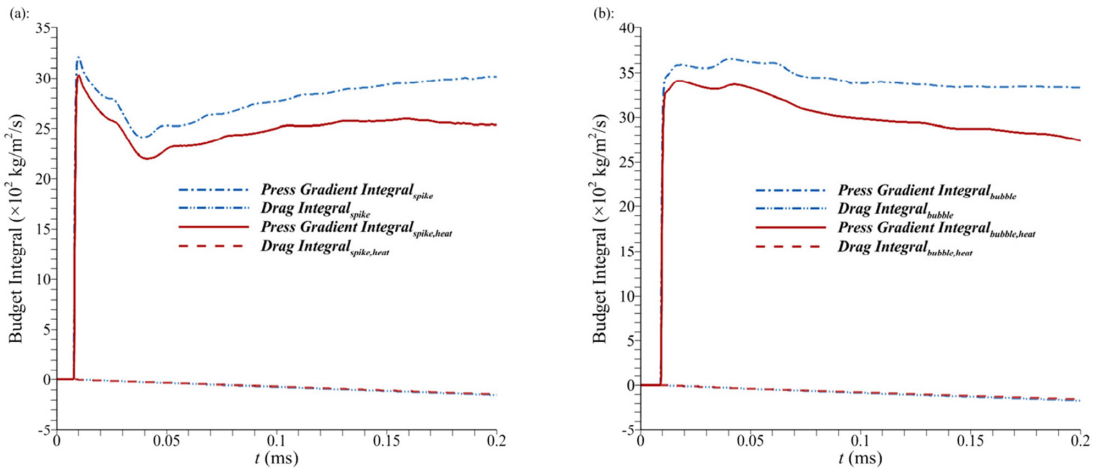

FIG. 16. Budget analysis of the integral form of the momentum equation at the (a) spike and (b) bubble in the heat transfer and non-heat transfer systems.

velocity of the bubble decreases faster than that of the spike, the growth rate of the mix zone decreases and the mix zone width decreases. Heat transfer is a form of energy dissipation. Microscopically, it is still the transmission of molecular kinetic energy, which is similar to viscosity.[47] In RMI problems, they both inhibit the growth of instability. However, they differ in the following aspects. First, viscosity can directly affect the fluid velocity by acting on the momentum equation, whereas heat transfer can only act on the energy equation. Second, interphase heat transfer can only occur in areas containing particles, whereas viscosity is present everywhere in fluids. Finally, if the particle temperature is higher than the fluid temperature, new results may be obtained.

VI. DISCUSSION AND VERIFICATION OF τ_T BY NUMERICAL SIMULATION

Through theoretical analysis, the dimensionless heat transfer relaxation time was used to characterize the heat transfer effect. This section demonstrates its accuracy and effectiveness using a numerical simulation. The expression for this dimensionless number includes the volume fraction, calculation conditions, particle properties, and fluid properties. These quantities are interrelated and cannot be simply split. Here, we only explore the effects of the particle volume fraction and temperature self-similarity. Verification was performed by considering several cases with different particle volume fractions and the same dimensionless number.

A. Comparison of different particle volume fractions

The above analysis demonstrates that the heat transfer reduces the movement velocity and growth rate of the mix zone. Combined with the dimensionless heat transfer relaxation time, we know that as the particle volume fraction increases, the influence of heat transfer on the mix zone increases, and the mix zone width decreases. To verify this hypothesis, we simulated the multiphase RMI with different particle volume fractions.

Keeping the rest of the conditions unchanged, the four cases with particle fractions of 0.01, 0.05, 0.1, and 0.2 were simulated in the heat transfer and non-heat transfer systems, and the growth rate changes of their mix zone widths were obtained, as shown in Fig. 18. The evolution of the mix zone width in the heat transfer systems with different particle volume fractions is presented in Fig. 19.

It can be seen that the above conclusions and influence mechanisms are also applicable to different particle volume fractions. First,

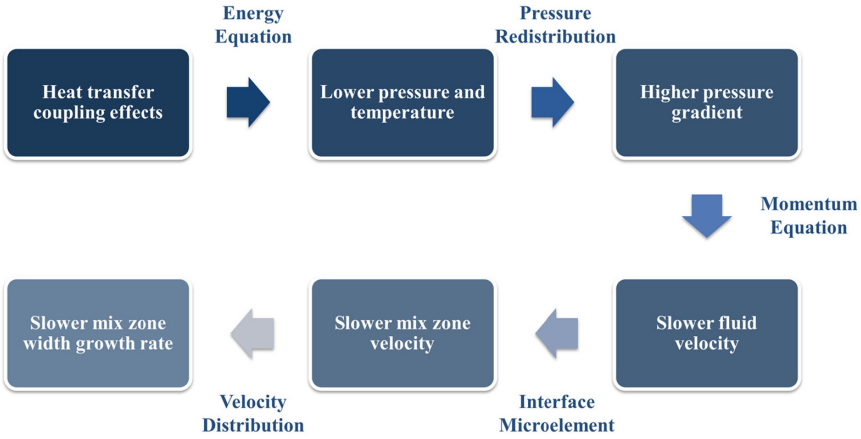

FIG. 17. Mechanism of the effects of heat transfer on the growth rate of the mix zone width.

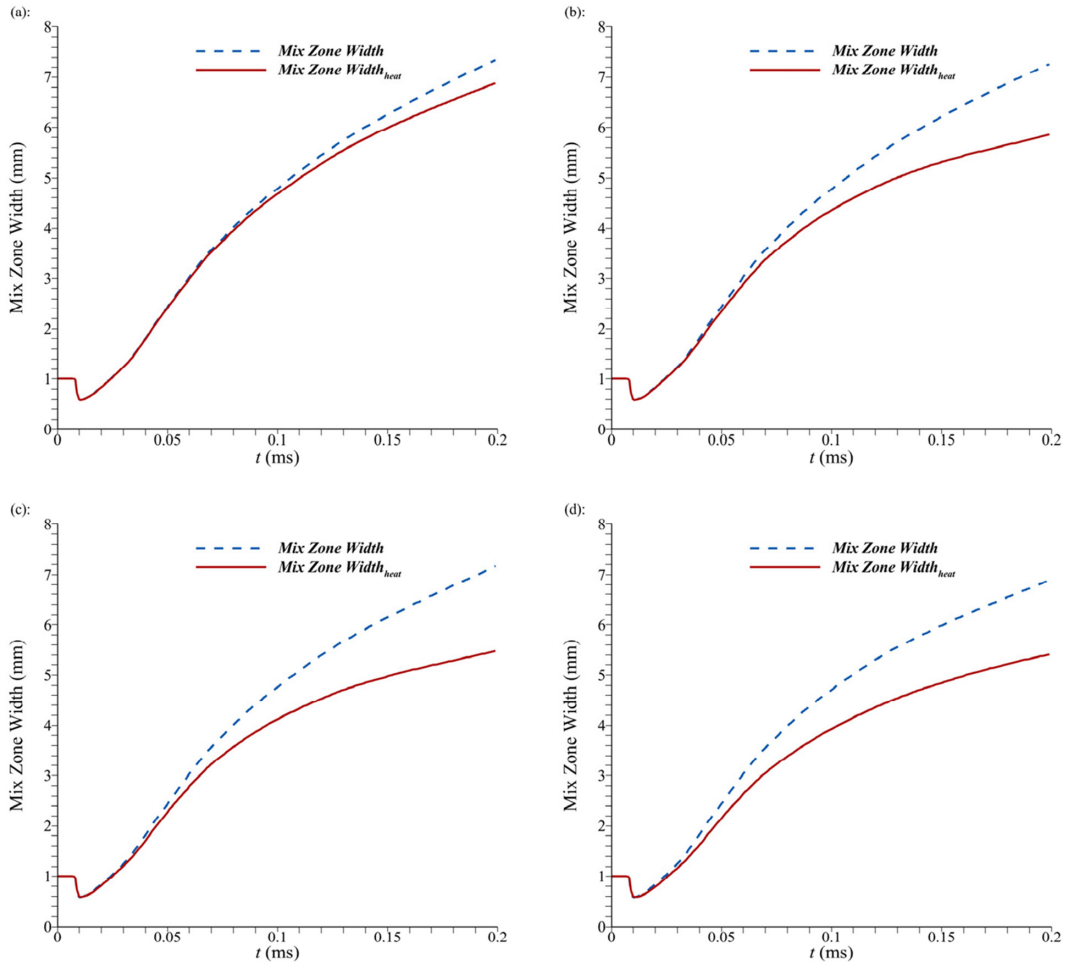

FIG. 18. Evolution of mix zone width in the heat transfer and non-heat transfer systems for particle volume fractions of (a) $\alpha_p = 0.01$, (b) $\alpha_p = 0.05$, (c) $\alpha_p = 0.1$, and (d) $\alpha_p = 0.2$.

owing to the large *St*, in the non-heat transfer system with different particle volume fractions, the drag effect of particles on the fluid is not obvious, and the variation curve of the mix zone width is relatively similar. Compared with the non-heat transfer system, as the particle volume fraction gradually increases, the mix zone width in the heat transfer system gradually decreases and its growth rate becomes slower. For $\alpha_p = 0.01$, the heat transfer between phases is slow; therefore, the heat transfer effect has little influence on the mix zone width. For $\alpha_p = 0.2$, the heat balance can be reached in a short time; therefore, the heat transfer effect has a relatively large influence on the mix zone width, and its growth rate also decreases significantly. However, continuing to increase the particle volume fraction does not cause the growth rate to decrease rapidly, and the influence on the mix zone width is close to saturation.

B. Temperature self-similarity in multiphase RMI

Similar to the Reynolds number, for two cases with the same dimensionless heat transfer relaxation time, we expect temperature self-similarity to be observed. For dimensionless time scales, the temperature variation trend and mix zone width should have a certain similarity.

In this study, the relaxation time of fluid heat transfer was approximately 0.6 ms, the characteristic time of shock propagation was approximately 0.3 ms, and the dimensionless heat transfer relaxation time was 2, which means that in the process of shock wave propagation, causing a large change in the fluid temperature is sufficient to affect the fluid velocity, and thereby to affect the mix zone and width growth rate. We extracted the images of the fluid temperature and particle temperature changes with time at the spike, as shown in Fig. 20. In the non-heat transfer system, the fluid temperature changes after the shock wave and finally remains stable; in the heat transfer system, the fluid temperature continues to decrease and finally approaches the particle temperature within the observation time. Owing to the large specific heat capacity of the particles, the temperature of the particles is almost maintained at the initial temperature in both the heat transfer and non-heat transfer systems.

To verify the dimensionless heat transfer times obtained further, we set up two cases and made them satisfy the conditions of a large *St* and heat transfer dominance in the energy equation. The condition

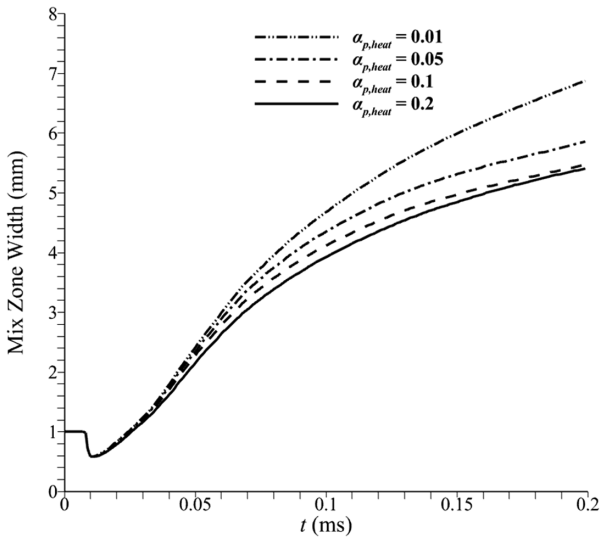

FIG. 19. Evolution of mix zone width in the heat transfer system for different particle volume fractions.

settings of case 1 are the same as above, and the new calculation example in case 2 adopts a smaller particle volume fraction and larger gas-phase thermal conductivity, to make the dimensionless numbers of the two sets of calculation examples as equal as possible. The relevant parameters for the two cases are listed in Table II. The temperature change and mix zone width curves of the two are shown in Figs. 21 and 22, respectively.

In the two cases with the same dimensionless number, the changing trends of the temperature and mix zone width are the same, and the values of these quantities are approximately equal. This finding indicates that the heat transfer has almost the same influence in the two cases, which also verifies the correctness and validity of the dimensionless heat transfer relaxation time.

TABLE II. Parameters for two cases.

	α_p	$H(\mathrm{mW/K})$	$t_T(\mathrm{ms})$	$t_c(\mathrm{ms})$	τ_T
Case 1	10%	0.579	0.613	0.295	2.07
Case 2	2.3%	0.275	0.608	0.295	2.06

VII. CONCLUSION

The objectives of this study were to investigate the influence of dense particle heat transfer on the fluid mix zone in a multiphase RMI problem and to derive the mechanism of the heat transfer effect. Theoretical analysis and numerical simulations using the CMP-PIC method were performed to improve the particle and gas phase equations, including the heat transfer effects.

The dimensionless number describing the heat transfer relaxation time was obtained by deriving the energy equation, which can characterize the effects of multiphase RMI heat transfer. When $\tau_T \gg 1$, the heat transfer can be ignored; when $\tau_T \sim 1$, the heat transfer effect needs to be considered in detail; and when $\tau_T \ll 1$, the heat balance is completed soon after contacting the particles, and the calculation is based on the physical quantities after the heat balance. For dense gas-particle flows or even granular flows, interphase heat transfer effects have very significant effects on the development of instabilities. The previous idea that the heat transfer effect is negligible is no longer applicable.

Based on the calculation results, we summarized the mechanism by which the interphase heat transfer affects the growth rate of the mix zone width. Heat transfer reduces the temperature and pressure in the particle-containing region, which affects the pressure gradient. Throughout the process, the pressure gradient has a much greater effect on the velocity than the drag, causing a major deceleration effect

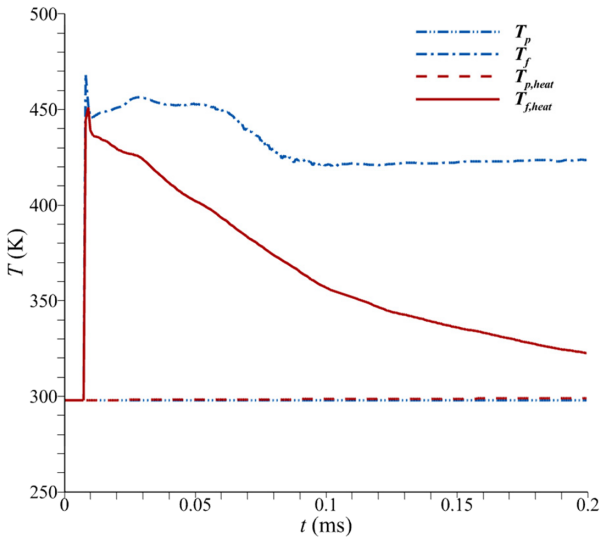

FIG. 20. Fluid and particle temperatures at the spike in the heat transfer and non-heat transfer systems.

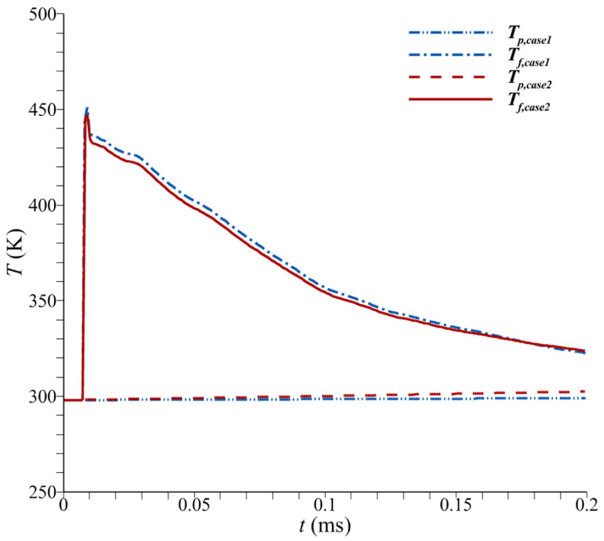

FIG. 21. Fluid and particle temperatures at the spike for two cases with the same dimensionless heat transfer relaxation time.

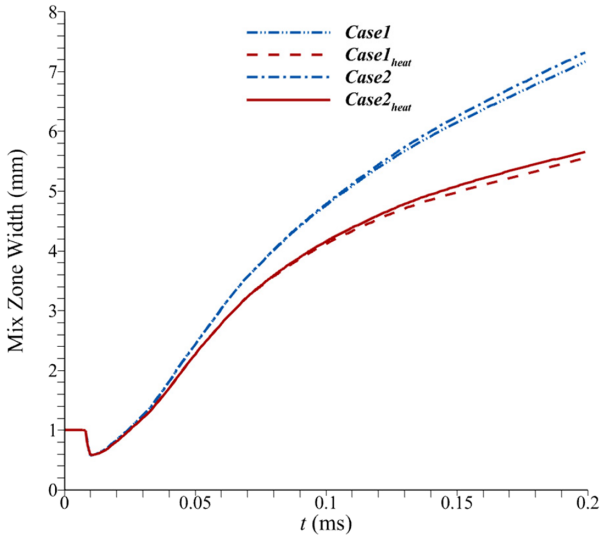

FIG. 22. Evolution of mix zone width for two cases with the same dimensionless heat transfer relaxation time.

on the fluid. Near the mix zone, the weakening of the right-going shock wave intensity is the main reason for the velocity reduction, which causes the mix zone in a heat transfer system to move more slowly than that in a non-heat transfer system. In addition, the speed of the bubble decreases faster than that of the spike, so the growth rate of the mix zone decreases and the mix zone width becomes smaller.

The above conclusions and influencing mechanisms are applicable to cases with different initial conditions. Compared with a non-heat transfer system, with a gradual increase in the particle volume fraction, the mix zone width in a heat transfer system gradually decreases, and its growth rate becomes slower. In the two cases, when the dimensionless numbers are the same, the variation trends of the temperature and mix zone width are basically the same. This characteristic shows the self-similarity of temperature and verifies the correctness and validity of the dimensionless heat transfer relaxation time.

The heat transfer effect has a great influence on the dense gas–particle flow, and the improved CMP-PIC method of the heat transfer model can provide a more accurate simulation for the engineering or natural phenomena of the dense particle multiphase flow. The related dimensionless number of heat transfer relaxation time can be used to predict the heat transfer effect of dense particles and provide guidance for experiments. In the future, we hope to continue to improve the gas–particle flow model with heat transfer and to simulate the heat transfer effect in multiphase RMI more precisely under different particle sizes and particle volume fractions. In addition, mass transfer and breakup models need to be incorporated to restore the evolution process of multiphase RMI accurately under actual conditions.

ACKNOWLEDGMENTS

Financial support from the National Natural Science Foundation of China (Grant Nos. 12002063, 12002062, 91852207, 12132017, and 12072353) and National Key Project (No. GJXM92579) are gratefully acknowledged.

AUTHOR DECLARATIONS

Conflict of Interest

The authors have no conflicts to disclose.

Author Contributions

Yingming Si: Conceptualization (equal); Data curation (equal); Formal analysis (equal); Investigation (equal); Methodology (equal); Project administration (equal); Resources (equal); Software (equal); Supervision (equal); Validation (equal); Visualization (equal); Writing – original draft (equal); Writing – review & editing (equal). **Shuai Li:** Resources (equal); Visualization (equal). **Qian Chen:** Funding acquisition (equal); Software (equal). **Baoqing Meng:** Conceptualization (equal); Formal analysis (equal); Funding acquisition (equal); Investigation (equal); Methodology (equal); Project administration (equal); Resources (equal); Software (equal); Supervision (equal). **Chun Wang:** Funding acquisition (equal); Resources (equal). **Baolin Tian:** Funding acquisition (equal); Project administration (equal).

DATA AVAILABILITY

The data that support the findings of this study are available from the corresponding authors upon reasonable request.

APPENDIX A: HEAT TRANSFER MODEL VALIDATION

To verify the correctness of the newly added heat transfer module, we simulated the gas–particle flow of single-particle one-way coupling heat transfer and compared the obtained particle temperature variations with the analytical results. For single-particle one-way coupling heat transfer, the governing equation of the particle temperature is

$$M_p C_{par} \frac{DT_p}{Dt} = Nu\pi \mathrm{d}_p k_f (T_f - T_p). \tag{A1}$$

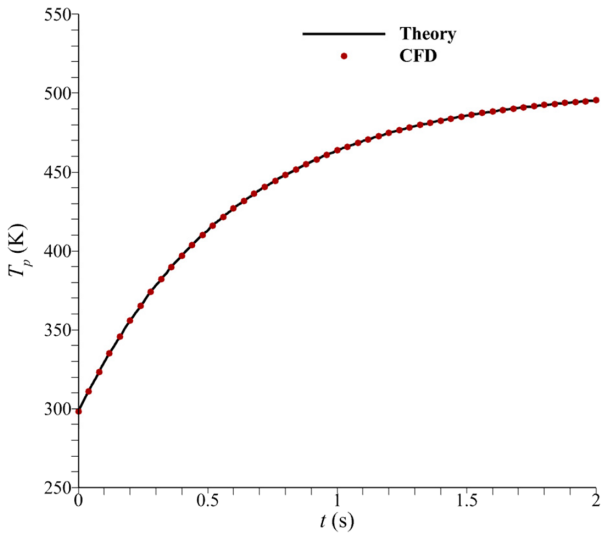

FIG. 23. Comparison of numerical and theoretical results for particle temperature.

Integrating Eq. (A1) and considering that when $t = 0$, $T_p = T_{p0}$, where T_{p0} is the initial temperature of the particle, yields

$$T_p = T_f - (T_f - T_{p0})e^{-\frac{Nu\pi d_p k_f}{M_p C_{par}}t}. \tag{A2}$$

In the verification example, the initial temperature of the particles was 298 K, and the incoming airflow was in the state after the shock wave of $Ma = 2$. Only the change in the particle temperature was considered, and the other conditions were set in the same manner as in Sec. IV A. The numerical and analytical results for the particle temperature are compared in Fig. 23. The numerical results agree well with the theoretical results, which verifies the correctness of the newly added heat transfer model.

When the thermal conductivity is zero, the model degenerates to the original CMP-PIC model and should be consistent with the theoretical solution. We compared the numerical results of the RMI simulations with the theoretical solution for the growth rate.[21] The cited study presents an RMI mix zone width linear segment model, as shown in Eqs. (A3) and (A4), which is suitable for low Ma and large St. Here, h is the width of the mix zone, k is the wave number of the disturbance interface, U_{inf0} is the interface velocity after the shock, a_0^+ is the disturbance amplitude after the shock, and t' is the time after the shock wave passes through the interface. A_{ls}^+ is the Atwood number after a shock at a large St, which is expressed in Eq. (A5), where ρ_{f1}^+ and ρ_{f2}^+ are the densities of gases 1 and 2 after the shock, respectively. Parameter $\bar{s}$ corresponds to the drag term and has units of frequency, as expressed in Eq. (A6),

$$\frac{dh}{dt} = 2kA_{ls}^+ U_{inf0} a_0^+ e^{-\bar{s}t'}, \tag{A3}$$

$$h = 2\frac{kA_{ls}^+ U_{inf0} a_0^+}{-\bar{s}}(e^{-\bar{s}t'} - 1) + h_0, \tag{A4}$$

$$A_{ls}^+ = \frac{\rho_{f2}^+ - \rho_{f1}^+}{\rho_{f2}^+ + \rho_{f1}^+}, \tag{A5}$$

TABLE III. Details of five grid resolutions.

	N_x	N_y	Total grid number	Total parcel number
Resolution A	200	25	5000	17 000
Resolution B	400	50	20 000	68 000
Resolution C	800	100	80 000	272 000
Resolution D	1600	200	320 000	1 088 000
Resolution E	2400	300	720 000	2 448 000

$$\bar{s} = \frac{\alpha_p \kappa}{2\alpha_f V_p}\left(\frac{1}{\rho_{f1}} + \frac{1}{\rho_{f2}}\right). \tag{A6}$$

Because the RMI linear segment growth rate model is only suitable for low Mach numbers to keep the fluid in an incompressible state after the shock wave, $Ma = 1.2$ was used in the verification example, and the rest of the condition settings were consistent with the above. The numerical results obtained from the simulation calculations and the analytical solutions given by the theoretical model are compared in Fig. 24. The numerical results are consistent with the theoretical results, verifying the correctness of the new CMP-PIC program.

APPENDIX B: GRID INDEPENDENCE VERIFICATION

We used five different grid resolutions to check the grid convergence, and the detailed data are listed in Table III. The other conditions were set in the same manner as in Sec. IV A. N_x and N_y are the resolutions in the x- and y-directions, respectively. Figure 25 shows a graph of the mix zone width as a function of time. The position of the interface was determined by the position of the volume fraction of gas 1, $\beta_1 = 0.5$. The mix zone width was measured from the peaks and valleys of the interface.

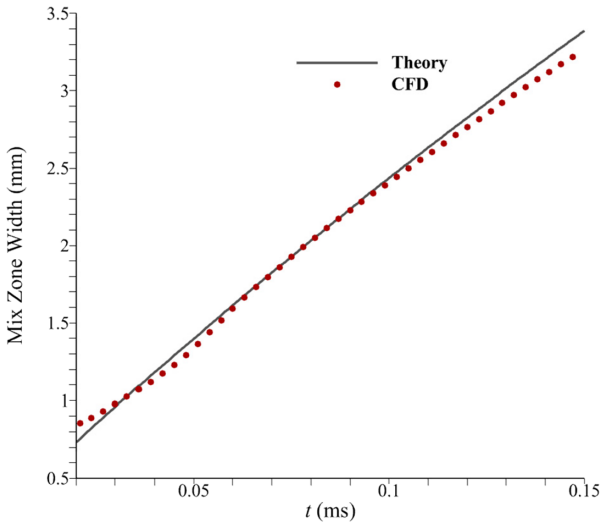

FIG. 24. Comparison of numerical and theoretical results for mix zone width.

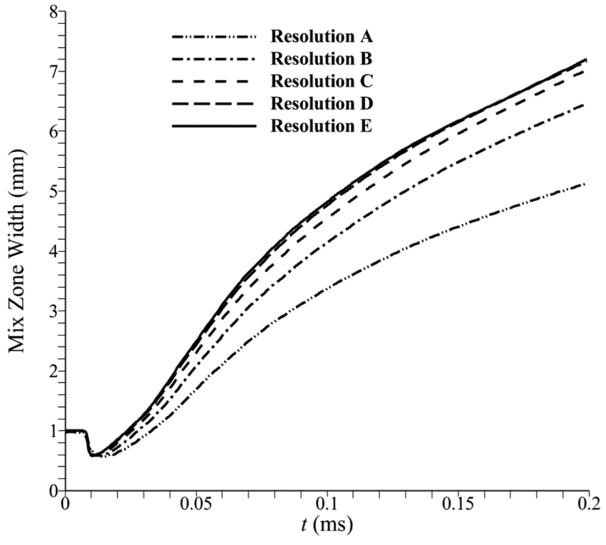

FIG. 25. Evolution of mix zone width for five resolutions.

The results for resolution D agree well with those for resolution E, indicating that continued refinement did not significantly affect the simulation. Therefore, resolution D was chosen for all subsequent simulations. It should be noted that each cell was assigned four parcels, which was demonstrated by Ukai *et al.* to achieve package resolution convergence.[2]

REFERENCES

[1]R. D. Richtmyer, "Taylor instability in shock acceleration of compressible fluids," Commun. Pure Appl. Math **13**(2), 297–319 (1960).
[2]S. Ukai, K. Balakrishnan, and S. Menon, "On Richtmyer-Meshkov instability in dilute gas-particle mixtures," Phys. Fluids **22**(10), 104103 (2010).
[3]X. S. Luo, M. H. Wang, T. Si *et al.*, "On the interaction of a planar shock with an SF_6 polygon," J. Fluid Mech. **773**, 366–394 (2015).
[4]X. S. Luo, G. Ben, Z. G. Zhai *et al.*, "Principal curvature effects on the early evolution of three-dimensional single-mode Richtmyer-Meshkov instabilities," Phys. Rev. E **93**(2), 023110 (2016).
[5]R. Sun, J. C. Ding, Z. G. Zhai *et al.*, "Convergent Richtmyer-Meshkov instability of heavy gas layer with perturbed inner surface," J. Fluid Mech. **902**, A3 (2020).
[6]Y. Zhou, W. H. Cabot, and B. Thornber, "Asymptotic behavior of the mixed mass in Rayleigh-Taylor and Richtmyer-Meshkov instability induced flows," Phys. Plasmas **23**(5), 052712 (2016).
[7]H. F. Li, Z. W. He, Y. S. Zhang *et al.*, "On the role of rarefaction/compression waves in Richtmyer-Meshkov instability with reshock," Phys. Fluids **31**(5), 054102 (2019).
[8]T. Sano, S. Tamatani, K. Matsuo *et al.*, "Laser astrophysics experiment on the amplification of magnetic fields by shock-induced interfacial instabilities," Phys. Rev. E **104**(3), 035206 (2021).
[9]L. F. Wang, W. H. Ye, X. T. He *et al.*, "Theoretical and simulation research of hydrodynamic instabilities in inertial-confinement fusion implosions," Sci. China Phys. Mech. Astron. **60**(5), 055201 (2017).
[10]D. T. Reese, A. M. Ames, C. D. Noble *et al.*, "Simultaneous direct measurements of concentration and velocity in the Richtmyer-Meshkov instability," J. Fluid Mech. **849**, 541–575 (2018).
[11]J. Yang, T. Kubota, and E. E. Zukoski, " Applications of shock-induced mixing to supersonic combustion," AIAA J. **31**(5), 854–862 (1993).
[12]Y. Luo, K. Luo, T. Jin *et al.*, "Fully resolved direct numerical simulation for shock/particle interaction," J. Eng. Thermophys. **37**(11), 2366–2371 (2016).
[13]J. Li, Y. Jiang, S. Z. Yu *et al.*, "Cooling effect of water injection on a high-temperature supersonic jet," Energies **8**(11), 13194–13210 (2015).
[14]C. Wang, G. Xiang, and Z. Jiang, "Theoretical approach to one-dimensional detonation instability," Appl. Math. Mech. **37**(9), 1231–1238 (2016).
[15]Z. B. Zhou, J. C. Ding, Z. G. Zhai *et al.*, "Mode coupling in converging Richtmyer-Meshkov instability of dual-mode interface," Acta Mech. Sin. **36**(2), 356–366 (2020).
[16]Y. B. Zhang, Z. B. Zhou, J. C. Ding *et al.*, "Interaction of a planar shock wave with two heavy/light interfaces," Acta Mech. Sin. **38**(9), 322047 (2022).
[17]Z. Zhai, L. Zou, Q. Wu *et al.*, "Review of experimental Richtmyer–Meshkov instability in shock tube: From simple to complex," Proc. Inst. Mech. Eng., Part C **232**(16), 2830–2849 (2018).
[18]F. Zhang, D. L. Frost, P. A. Thibault *et al.*, "Explosive dispersal of solid particles," Shock Waves **10**(6), 431–443 (2001).
[19]P. G. Saffman, "On the stability of laminar flow of a dusty gas," J. Fluid Mech. **13**(1), 120–128 (1962).
[20]B. Q. Meng, J. S. Zeng, B. L. Tian *et al.*, "Modeling and verification of the Richtmyer-Meshkov instability linear growth rate of the dense gas-particle flow," Phys. Fluids **31**(7), 074102 (2019).
[21]B. Q. Meng, J. S. Zeng, B. L. Tian *et al.*, "Modeling and simulation of a single-mode multiphase Richtmyer-Meshkov instability with a large Stokes number," AIP Adv. **9**(12), 125311 (2019).
[22]H. Zheng, Q. Chen, B. Q. Meng *et al.*, "On the nonlinear growth of multiphase Richtmyer-Meshkov instability in dilute gas-particles flow," Chin. Phys. Lett. **37**(1), 015201 (2020).
[23]J. A. Mcfarland, W. J. Black, J. Dahal *et al.*, "Computational study of the shock driven instability of a multiphase particle-gas system," Phys. Fluids **28**(2), 024105 (2016).
[24]J. C. Schulz, K. C. Gottiparthi, and S. Menon, "Richtmyer-Meshkov instability in dilute gas-particle mixtures with re-shock," Phys. Fluids **25**(11), 114105 (2013).
[25]Y. Bin, M. Xiao, Y. Shi *et al.*, "A new idea to predict reshocked Richtmyer–Meshkov mixing: Constrained large-eddy simulation," J. Fluid Mech. **918**, R1 (2021).
[26]V. Duke-Walker, W. C. Maxon, S. R. Zlmuhna *et al.*, "Evaporation and breakup effects in the shock-driven multiphase instability," J. Fluid Mech. **908**, A13 (2021).
[27]H. W. J. Goosens, J. W. Cleijne, H. J. Smolders *et al.*, "Shock-wave induced evaporation of water droplets in a gas-droplet mixture," Exp. Fluids **6**(8), 561–568 (1988).
[28]S. Huang, J. Zhang, J. Ding *et al.*, "Richtmyer–Meshkov instability with ionization at extreme impact conditions," Phys. Fluids **34**(7), 072101 (2022).
[29]S. Sundaresan, A. Ozel, and J. Kolehmainen, "Toward constitutive models for momentum, species, and energy transport in gas-particle flows," Ann. Rev. Chem. Biol. Eng. **9**, 61–81 (2018).
[30]J. A. Mcfarland and M. Magenmaier, "Computational study of shock-driven multiphase mixing in scramjet conditions," AIAA J. **56**(10), 4004–4015 (2018).
[31]B. L. Tian, J. S. Zeng, B. Q. Meng *et al.*, "Compressible multiphase particle-in-cell method (CMP-PIC) for full pattern flows of gas-particle system," J. Comput. Phys. **418**, 109602 (2020).
[32]M. J. Andrews and P. J. Orourke, "The multiphase particle-in-cell (MP-PIC) method for dense particulate flows," Int. J. Multiphase Flow **22**(2), 379–402 (1996).
[33]F. Alobaid and B. Epple, "Improvement, validation and application of CFD/DEM model to dense gas-solid flow in a fluidized bed," Particuology **11**(5), 514–526 (2013).
[34]D. D. Xu, F. Yang, H. H. Jin *et al.*, "An investigation of heat transfer of flexible fibres in a rotating drum dryer using the discrete element method," Powder Technol. **364**, 494–506 (2020).
[35]D. L. Shi, W. L. Vargas, and J. J. Mccarthy, "Heat transfer in rotary kilns with interstitial gases," Chem. Eng. Sci. **63**(18), 4506–4516 (2008).
[36]N. Gui, J. Yan, W. K. Xu *et al.*, "DEM simulation and analysis of particle mixing and heat conduction in a rotating drum," Chem. Eng. Sci. **97**, 225–234 (2013).
[37]C. T. Crowe, J. D. Schwarzkopf, M. Sommerfeld *et al.*, *Multiphase Flows with Droplets and Particles*, 2nd ed. (CRC Press, Boca Raton, FL, 2012).
[38]W. E. Ranz and W. R. Marshall, "Evaporation from drops," Chem. Eng. Prog. **48**(3), 141–146 (1952).
[39]C. W. Shu and S. Osher, "Efficient implementation of essentially non-oscillatory shock-capturing schemes," J. Comput. Phys. **77**(2), 439–471 (1988).
[40]A. Harten, P. D. Lax, and B. Van Leer, "On upstream differencing and Godunov-type schemes for hyperbolic conservation-laws," SIAM Rev. **25**(1), 35–61 (1983).
[41]B. Q. Meng, J. S. Zeng, Q. Chen *et al.*, "Numerical method for compressible gas-particle flow coupling using adaptive parcel refinement (APR) method on non-uniform mesh," J. Comput. Phys. **466**, 111418 (2022).
[42]S. J. Reckinger, D. Livescu, and O. V. Vasilyev, "Adaptive wavelet collocation method simulations of Rayleigh-Taylor instability," Phys. Scr. **T142**, 014064 (2010).
[43]S. Singh, "Contribution of Mach number to the evolution of the Richtmyer-Meshkov instability induced by a shock-accelerated square light bubble," Phys. Rev. Fluids **6**(10), 104001 (2021).
[44]S. Singh, M. Battiato, and R. S. Myong, "Impact of bulk viscosity on flow morphology of shock-accelerated cylindrical light bubble in diatomic and polyatomic gases," Phys. Fluids **33**(6), 066103 (2021).
[45]S. Singh and M. Battiato, "Numerical simulations of Richtmyer–Meshkov instability of SF_6 square bubble in diatomic and polyatomic gases," Comput. Fluids **242**, 105502 (2022).
[46]S. Singh and M. Torrilhon, "On the shock-driven hydrodynamic instability in square and rectangular light gas bubbles: A comparative study from numerical simulations," Phys. Fluids **35**(1), 012117 (2023).
[47]P. Sun, J. Ding, S. Huang *et al.*, "Microscopic Richtmyer–Meshkov instability under strong shock," Phys. Fluids **32**(2), 024109 (2020).